Rate Effects in Mode-II Fracture of Plastically Deforming, Adhesively-Bonded Structures

C. Sun[a], M. D. Thouless[b, c], A. M. Waas,[a, b] J. A. Schroeder[d] and P. D. Zavattieri[d]

[a]*Department of Aerospace Engineering*
[b]*Department of Mechanical Engineering*
[c]*Department of Materials Science and Engineering,*
University of Michigan, Ann Arbor, MI 48109, USA

[d]*General Motors Research and Development, 30500 Mound Rd., Warren, MI 48090, USA*

ABSTRACT

Results from a combined experimental and numerical investigation into the effects of rate on mode-II fracture of a plastically-deforming, adhesively-bonded joint are presented. It is shown that a cohesive-zone model has to be modified to include coupling between normal and shear modes of deformation when there is extensive shear deformation of the adhesive layer. A suitable cohesive-zone modeling strategy is described, and the mode-II cohesive parameters determined from the model are presented as a function of loading rate. Previous studies of the same system showed that the effects of rate in mode-I were limited to the probability that a crack growing in a toughened quasi-static mode would spontaneously make a transition to a brittle mode of fracture. No such transitions were found for mode-II fracture. Crack growth always occurred in a quasi-static fashion. While there was some evidence that rate might affect the mode-II fracture parameters, these effects were very limited even up to crack velocities of about 1000 mm/s. Any possible effects was limited to a very minor increase in toughness and strength with increased loading rates. However. the magnitude of these possible increases were comparable to the magnitude of the uncertainties in the measured values.

(February 19, 2009)

1. INTRODUCTION

Adhesive bonding exhibits many advantages over traditional joining techniques for automotive applications. These include reductions in weight and, hence, an increase in fuel efficiency. However, the current use of adhesive bonding in the automotive industry is limited because of the lack of a suitable design methodology. The present research is part of an on-going effort to develop such a methodology, with an emphasis on determining mixed-mode cohesive parameters as a function of loading rate. Earlier work of Sun *et al.* [2008a, 2008b] explored the effects of rate on mode-I fracture of plastically-deforming, adhesively-bonded sheet metal. The specimens in that study failed either by fully-toughened quasi-static crack growth, or by a "stick-slip" type of behavior with quasi-static crack growth being interrupted by intermittent periods of relatively brittle dynamic fracture. The experiments indicated that the cohesive parameters for mode-I quasi-static crack growth were independent of rate, and that quasi-static crack growth could occur even at crack velocities as high as several meters per second. Effects of rate appeared to be limited to the ease with which a transition to dynamic fracture could be triggered. The present paper extends the study to mode-II, whilst a companion paper [Sun *et al.*, 2008c] demonstrates how the mode-I and mode-II parameters can be combined to explore mixed-mode fracture at different rates.

There is a long history of studying mode-II fracture in adhesive joints [Chai, 1988]. Much of this work has focused on the use of linear-elastic fracture mechanics (LEFM) to develop geometries to measure the mode-II toughness [Carlsson *et al.*. 1986; Edde *et al*., 2001; Qiao *et al.* 2003; Blackman *et al.*, 2006], and on the effects of friction during mode-II fracture [Bulchholz *et al*., 1997; Fernlund *et al*. 2001; Schuecker *et al*.,

2001; Sun and Davidson 2006]. In related work, LEFM techniques have also been used to investigate the effects of rate on the mode-II fracture of composite structures [Jacob *et al.,* 2005]. It is noted that no unambiguous relationship between rate and the mode-II toughness resulted from these studies, with different studies showing either increases, decreases or no effect of rate on toughness [Caimmi *et al.*, 2006; Giambanco *et al.*, 2006; Liechti and Wu*,* 2001].

Cohesive models of fracture [Ungsuwarungsri and Knauss, 1987; Tvergaard and Hutchinson, 1992], provide additional flexibility for fracture analysis by the introduction of a characteristic strength. Applying a cohesive-zone modeling strategy to adhesive joints by identifying the cohesive parameters with the deformation of the entire adhesive layer, permits fracture to be analyzed in situations which cannot be described by LEFM. In particular, it is possible to model fracture when there is plasticity in the adherends [Yang *et al.*, 1999]. The major issue is the identification of the cohesive parameters. Two general approaches to determine the cohesive properties and the traction-separation laws of adhesive joints have evolved in the literature. In one approach, based on the *J*-integral, a linear-elastic geometry is used and the *J*-integral is calculated from the geometry and loads or displacements. This value of *J*-integral is plotted as a function of the crack-opening displacement, and the slope is taken as a measure of the crack-tip tractions. Examples of this approach for mode-II studies are given by Leffler *et al.* [2007] and Zhu *et al.* [2009]. While this approach gives a rigorous result for the shear tractions as a function of shear displacement, geometries for which the *J*-integral is valid are, by definition, geometries that are not sensitive to the magnitude of the cohesive tractions. Furthermore, it is not obvious that cohesive parameters must remain

unchanged between conditions under which they can be determined by use of the *J*-integral and conditions under which the *J*-integral may not be valid, such as in a plastically deforming structure. An alternative approach in which the fracture behavior is matched empirically to numerical predictions based on different cohesive parameters [Yang *et al.,* 2001] avoids this potential problem. However, this latter approach requires a recognition that there may be multiple sets of cohesive laws that provide fits to single sets of data [Sun *et al*., 2008b]; multiple experimental observations are then generally required to identify a unique set of parameters that describes the physical attributes of the adhesive layer.

The present paper uses a cohesive-zone approach to explore the effects of rate, up to low-velocity impact loading, for mode-II fracture of plastically-deforming adhesive joints. A series of experimental observations are described from which the mode-II cohesive parameters are determined. In addition, issues associated with modeling shear by means of a cohesive-zone model are described. In particular, it is shown that when the adhesive layer is relatively thick and the shear strains are relatively large, coupling of the normal and shear modes of deformation may be required to describe the behavior of the adhesive layer with sufficient accuracy. A modified cohesive model is developed and used to determine mode-II cohesive-zone parameters as a function of loading rate. These parameters have subsequently been used in a companion paper to model mixed-mode fracture [Sun *et al.*, 2008c].

2. EXPERIMENTAL RESULTS

The steel/adhesive/steel specimens used in this research were made by bonding coupons of a dual-phase steel with a layer of a commercial, rubber-toughened, epoxy-

based adhesive cured at 180 ºC for thirty minutes. The thickness of the adhesive layer was fixed at 0.8 mm by means of incorporating glass beads into the adhesive. The properties of the steel coupons (after the curing schedule) and of the bulk adhesive have been summarized in a previous paper [Sun *et al.*, 2008a].

2.1 Three-point-bending, end-notched-flexure tests

The deformation at the tip of a crack in an edge-notched-flexure (ENF) specimen is dominated by shear. Therefore, this geometry provides an excellent configuration to study mode-II fracture with elastic [Barrett and Foschi, 1977; Carlsson *et al.*, 1986] and plastic deformation [Yang *et al.*, 2001]. The geometry of the ENF specimens used in this study is shown in Fig. 1. A steel wire with a diameter of about 0.8 mm was inserted as a spacer between the steel arms at the crack mouth. Teflon® tape was used to define the initial extent of the crack, and a scale was attached to the side of the specimens. The specimens were tested in a servo-hydraulic machine under displacement control. Four tests at a loading rate of 0.1 mm/s, 4 tests at a rate of 10 mm/s, and 5 tests at a rate of 200 mm/s were performed. A high-resolution CCD camera was used to monitor crack propagation and to calibrate the cross-head displacement.

An example of the optical micrographs taken during the tests is shown in Fig. 2. These optical observations and visual inspections of the specimens after testing confirmed that the crack always propagated at (or close to) the interface between the adhesive and the top adherend (the arm onto which the central load was applied). This interfacial mode of failure resulted from the mode-II loading on the specimen, and was in contrast to the failure observed in pure mode-I, where the crack ran through the middle of the adhesive layer. A crack trajectory along the top interface is consistent with what

would be predicted from a linear-elastic fracture mechanics analysis of the ENF geometry. In some specimens, the initial defect lay along the top interface along which it eventually propagated. In other specimens (as in Fig. 2), the initial defect lay along the bottom interface and a kink formed to the top interface. Since the mode-II toughness of the interface was much higher than the mode-I toughness of the adhesive, any kink from the bottom surface was arrested at the top interface until the load increased to a sufficient level for subsequent mode-II delamination to occur.

Plots of the applied load against mid-point deflection are shown in Fig. 3. As indicated on the plots, the cracks were observed to start growing along the top interface just before the peak load. However, as observed in other three-point bending tests [Leffler *et al.*, 2007] there was no obvious effect of this delamination on the load-displacement behavior. The onset of any kinking has also been indicated on Fig. 3. As discussed above, this occurred at lower loads than those associated with interfacial delamination. Figure 3 suggests there may be a small rate effect on the relationship between load and displacement. However, this figure shows no evidence of the ductile-to-brittle transitions ("stick-slip") observed in mode-I for this system [Sun *et al.*, 2008a]. Nor was there any evidence of this type of transition on the fracture surfaces.

Plots of crack extension as a function of time after the cracks began to grow are given in Fig. 4. These plots are consistent with quasi-static crack growth and only very limited rate effects, as confirmed by the observation that the crack velocities scale approximately with the applied displacement rate. The average crack velocities were 0.24 ± 0.06 mm/s, 20 ± 2 mm/s and 350 ± 90 mm/s for applied displacement rates of 0.1 mm/s, 10 mm/s and 200 mm/s, respectively.

2.2 Clamped, end-notched flexure tests

Clamped, end-notched flexure specimens were tested using a drop tower to provide high loading rates. These specimens were fabricated in exactly the same fashion as the earlier specimens, and the dimensions are given in Fig. 5. The specimens were clamped in the top of a fixture, machined and hardened from a 4141-steel, by means of a steel block held in place by set screws. An optical micrograph of the experimental configuration is shown in Fig. 6. The tests were conducted by dropping a steel cylinder with a diameter of 12 ± 0.5 mm attached to a test weight with a mass of 40 kg onto the specimens from different heights of between 30 and 1000 mm. The distance from the clamp to the loading point on the specimens was 30 ± 1 mm, and the initial crack length was 10 ± 1 mm from this point (Fig. 5). A high-speed camera[1] was focused on a scale scribed on the side of the specimen. This allowed the positions of the crack tip and the displacement of the loading point to be monitored as a function of time. The load transmitted to the specimen was monitored by means of a load cell placed between the cylinder and the drop weight. The signal from the load cell was recorded by an oscilloscope. The camera was triggered after a fixed delay of 1 μs from when the initial signal from the impact was received. Figure 7 shows that the velocity of the loading point was essentially constant through the entire experiment, except at the lowest loading rate. The average loading velocities were 900 ± 50 mm/s, 1800 ± 100 mm/s and 4200 ± 50 mm/s for drop heights of 50 mm, 200 mm and 1000 mm, respectively. The velocity of the loading point varied between about 300 mm/s and 600 mm/s for a drop height of 30 mm.

[1] A Cordin Model 220 gated, intensified CCD camera. This system could capture a maximum of 12 images in 120 ns, when needed.

A typical plot of the raw data for the reaction load and deflection of the loading point is shown in Fig. 8, for a test with a drop height of 200 mm. These data were then filtered digitally by using a discrete Fourier transform to remove the high frequencies that appear to correspond to the natural frequency of the clamped beam. This resulted in a relatively smooth curve load-displacement curve that has been added to Fig. 8 for comparison. A complete set of all the test data, after smoothing by this procedure, is presented in Fig. 9. Although the data from the different tests show a considerable spread, there was no obviously consistent effect of rate on these load-displacement traces over the range of crack velocities studied. The onset of kinking and the onset of interfacial crack propagation have been indicated on the load-displacement plots of Fig. 9. There was no obvious effect on the load-displacement plots from either event. One significant difference observed between the clamped and simply-supported geometries was that crack propagation began *after* the peak load for the clamped geometry, but *before* the peak load for the simply-supported geometry.

From a mechanics perspective, this clamped ENF geometry is similar to the simply-supported geometry. However, it differs in one respect: the clamping provides a nominal plane of symmetry for the specimen that is missing from a simply-supported specimen with a single crack. This difference, in conjunction with the relatively large deflections associated with plastic deformation during these tests can influence the behavior of the specimens. The other differences between the two geometries are merely cosmetic. The clamped geometry is inverted, so that the sense of the mode-II component of the energy-release rate drives the crack along the interface between the adhesive and the *bottom* adherend. This can be seen from the micrograph of Fig. 11, which shows a

crack kinking through the adhesive to the bottom interface. Finally, it should be noted that, all else being equal, the loads for the simply-supported geometry would be expected to be approximately double those for the clamped geometry (because of where the load is measured).

Plots of the crack extension against time are shown in Fig. 11. From these data, the crack velocities were determined to be approximately 300 ± 60 mm/s, 500 ± 80 mm/s, 1100 ±100 mm/s and 2400 ± 300 mm/s for drop heights of 30 mm, 50 mm, 200 mm and 1000 mm, respectively. As in the lower-rate tests, there was no evidence of any stick-slip behavior in mode-II. This is a significant contrast to the behavior under mode-I conditions for this system [Sun *et al.* 2008a], and suggests that different toughening modes may be operating in the two modes of fracture.

For completeness, companion tests with the clamped geometry were conducted using a servo-hydraulic machine under displacement control at rates of 0.1 mm/s and 200 mm/s. One significant difference was observed between these tests and the clamped ENF tests performed under impact conditions: the nature of the plastic deformation was different. As can be seen from the micrographs of Fig. 12, a plastic hinge was formed near the crack tip in the drop-tower tests, and a plastic hinge formed near the clamped root of the specimen in the servo-hydraulic machine tests. Further investigation of this phenomenon indicated that it was a robust experimental observation, and it was not dependent on uncertainties in the boundary conditions or in the details of the loading. As will be discussed in the numerical section, it is believed that the phenomenon is associated with a subtle effect of loading rate on the material properties of the adhesive layer.

2.3 Lap-shear tests

The single-lap shear geometry is often used to examine mixed-mode crack propagation. However, cohesive-zone calculations indicated that fracture can depend only on the mode-II cohesive strength, and not on the mode-II toughness or the mode-I parameters, if the overlap length is kept relatively short. Therefore, specimens with such a geometry (Fig. 13) were used to explore whether they could provide a value of the cohesive shear strength of the interface. These specimens provided an analogous test to that used in the earlier work [Sun *et al.*, 2008b] to determine the mode-I cohesive strength for this adhesive system.

The specimens were fabricated following the same protocol as used for all the other specimens in this project; in particular, the thickness of the adhesive layer was kept at 0.8 mm. Four tests were conducted at each of three different cross-head displacement rates (0.01 mm/s, 10 mm/s and 200 mm/s) in a servo-hydraulic machine. Crack propagation in all tests was interfacial, with the fracture surfaces very similar to those observed in the ENF tests. The crack growth was too rapid to be observed optically, owing to the difficulty in establishing a suitable trigger to capture the event with an appropriate time resolution. The nominal shear strength of the bond was determined by dividing the maximum load supported by the area of the adhesive. This quantity was equal to 27 ± 3 MPa, 32 ± 3 MPa and 34 ± 3 MPa corresponding to displacement rates of 0.01 mm/s, 10 mm/s and 200 mm/s respectively. Based on cohesive-zone models of this geometry, these values could be taken to be the mode-II cohesive strengths of the adhesive system. As will be demonstrated subsequently, these values were consistent with the cohesive strengths obtained independently from the ENF tests.

3. NUMERICAL RESULTS

3.1 Numerical simulations for the three-point-bending, ENF geometry

3.1.1 Continuum calculations

A finite-element calculation using the continuum properties of the adhesive was performed to explore the evolution of the stresses in the adhesive layer prior to the propagation of the crack (Fig. 14). This was implemented for the ENF geometry using an ABAQUS/Standard 2D model, with the dimensions given in Fig. 1. Both the adherends and the adhesive were represented by four-node, plane-strain elements. While only a single layer of elements was used for the 0.8 mm thickness of the adhesive layer, a subsequent mesh-refinement analysis verified that the numerical results were essentially unchanged by the use of finer meshes. To prevent interpenetration at the crack mouth, surface-based contact elements were used to simulate both the interaction between the steel spacer and the two arms. Contact elements were also used to simulate the interaction between the specimen and the three rollers. The coefficient of friction between steel and steel was assumed to be 0.8; however, numerical calculations indicated that the precise value for this parameter did not significantly affect the results. The properties of the steel adherends and of the adhesive layer were described by point-to-point representations of the uniaxial stress-strain curves given in Sun *et al*. [2008a]. Isotropic properties, with a von Mises yield criterion and isotropic hardening were assumed for both materials. An initial strain rate for the adhesive was assumed so that the appropriate constitutive properties could be used. It was subsequently verified that this assumed rate was consistent with the results of the numerical calculations.

Figure 16 shows a comparison between the load *versus* mid-point deflection plots obtained numerically and experimentally at an applied displacement rate of 0.1 mm/s.

Good agreement between the two is seen until the peak load in the numerical plot. The shear-strain rate at the crack tip was determined to be about $0.0115\ s^{-1}$ by dividing increments of the calculated shear displacement across the adhesive layer by the associated increments of applied displacement, and taking the displacement rate to be 0.1 mm/s. It was this calculated strain rate that was verified as being consistent with the constitutive properties used for the adhesive in the numerical model. As commented upon earlier, crack propagation was observed before the peak load,[2] therefore, the calculations of Fig. 15 indicate that the continuum calculations describe the load-displacement behavior even after the onset of crack propagation. This implies that significant frictional effects allowed the full load-bearing capacity of the adhesive layer to be continued even after crack growth had commenced. Indeed, the frictional stress must have been comparable to the yield strength of the adhesive layer during the initial stages of crack propagation for the load to continue tracking with the continuum predictions. The peak load in the load-displacement plot must indicate the point at which the frictional stresses started to drop from this high level.

A plot of shear stress against shear strain for the adhesive was obtained by tracking the stress-strain behavior of the element representing the adhesive at the crack tip. This curve is shown in Fig. 16. If the co-ordinate axis of this figure were to be converted to displacement (rather than strain), the curve could then be taken to represent the mode-II cohesive law up to the point of softening.[3] This figure indicates that the

---

[2] Observations of the fracture surface indicated that the crack advanced further in the middle of the adhesive, than at the edges. Therefore, the observations of crack advance before the peak load were not just a surface phenomenon.

[3] The agreement between the continuum calculations and the experimental curve in Fig. 15 implies that the deformation mechanism of the adhesive layer is not affected by the constraints of the adherends.

shear strength exhibited by the adhesive at an applied displacement rate of 0.1 mm/s is about 21 MPa, and that the shear modulus of the adhesive at this rate is about 350 MPa. These continuum calculations were repeated for the tests conducted at higher displacement rates. For tests with a mid-point deflection rate of 200 mm/s, the shear strain rate at the crack tip in adhesive layer was calculated to be as high as up to 20 /s. This shear strain rate corresponds to a higher normal strain rate than had been obtained in the uniaxial tensile tests described in Sun *et al*. [2008a]. Therefore, the appropriate shear modulus could only be estimated by extrapolation of the tensile data. It was estimated to be about 520 MPa. The results of the numerical calculations for the ENF tests using this value of shear modulus were not inconsistent with the experimental results.

3.1.2 Cohesive-zone model

As described in the Appendix, an initial attempt to use the cohesive-zone model of Li *et al*. [2006] failed to provide agreement with the experimental results. This original model was one that did not couple the shear and normal modes of deformation. Such an approximation appears to be satisfactory when there are limited shear strains or when the thickness of the adhesive layer is very much less than the thickness of the adherends. It was apparent that the problem in the present case resided in the numerical formulation not in the choice of constitutive properties of the adhesive layer. The Appendix describes a new formulation for the cohesive-zone model that couples the shear and normal displacements of the nodes in the cohesive-zone to resolve this discrepancy.

The characteristic traction-separation laws used to describe the behavior of the adhesive layer are shown in Fig. A1. These are approximate representations for the elastic-plastic behavior such as that shown in Fig. 16. Although the geometries presented

in this paper are all nominally pure mode-II geometries, a mixed-mode formulation of the cohesive-zone model was used to ensure a general model.[4] The mode-I cohesive parameters were taken to be the quasi-static mode-I law obtained in the prior work on this system [Sun *et al.*, 2008b]. The mode-II parameters were determined by a process of fits between numerical results and specific features of the experimental results at different loading rates. The process is described below using one specific experimental example at a loading rate of 0.1 mm/s. This process was repeated for every set of experimental data at different rates to determine the ranges of uncertainty and the effects of rate.

First, the initial slope of the cohesive law was obtained from the shear modulus of the adhesive layer. The properties of the adhesive, as determined by a tensile test [Sun *et al.*, 2008a], were incorporated within a continuum numerical model of the ENF test. It was verified that the strain rate was consistent with the properties, and that the elastic slope of the load-displacement curve for the ENF test was correct. Then the shear modulus and the thickness of the adhesive layer were used to determine the initial slope of the mode-II law to give the correct compliance of the adhesive layer. For example, as discussed above. the shear modulus of the adhesive layer was 350 MPa at displacement rate of 0.1 mm/s (Fig. 16) which, for an adhesive layer of 0.8 mm thick, translates to an initial slope of 440 MPa/mm.

Second, the mode-II cohesive strength, $\hat{\tau}$, was determined by numerical matches to the portion of the experimental load-displacement curves immediately after the

[4] The mode-I law developed in Sun *et al*. (2008b) was for a crack within the adhesive layer. In this geometry, mode-II cracks always grew along the interface. Sensitivity analyses were conducted to confirm that the results in this paper were insensitive to the choice of mode-I cohesive laws. Subsequent work has identified the appropriate mode-I cohesive laws for interfacial failure (Sun *et al.,* 2008c), and it was verified that the use of the more correct laws did not affect the present results.

deviation from linearity induced by plastic flow of the adhesive and steel.[5] Figure 17 shows the sensitivity to minor changes in this cohesive strength, keeping the total area under the curve and the unloading slope of the traction-separation law fixed. For an applied displacement rate of 0.1 mm/s, the shear cohesive strength was determined to be 23 ± 2 MPa. Within the uncertainty levels, this is consistent with the results from the continuum calculation presented above. It is also consistent with the results obtained from the lower-rate tests conducted with the lap-shear geometry.

Third, the critical displacement for the onset of crack growth, δ_{tc} (Fig. A1), was obtained by determining the point on the experimental load-displacement curve at which crack propagation was observed optically. Identifying this with the equivalent point on the numerical load-displacement curve, allowed the area traced out under the traction-separation law up to this point to be determined from the cohesive strength. This area is associated with the mode-II toughness of the adhesive layer, as indicated in Fig. A1. For an applied displacement rate of 0.1 mm/s, the critical shear displacement was calculated to be 0.50 ± 0.05 mm. This corresponded to a mode-II toughness of 11 ± 1 kJ/m^2.

Fourth, the characteristics of the frictional portion of the traction-separation law were evaluated. The critical displacement at which the traction-separation law unloads, δ_{t2}, was determined from the peak load. By varying this displacement in the numerical model until the calculated peak load matched the experimental peak load, it was

[5] Different forms of non-linear plastic flow that the adhesive might exhibit did not seem to be a major factor in determining the shape of the load-displacement curve. The characteristic strength seemed to be the important parameter for capturing the behavior of this portion of the curve. In other words, the simple form of Fig. 1 was sufficient for these purposes. There was no need to mimic the precise shape of the traction-separation curve illustrated in Fig. 17 that was obtained from considerations of the continuum properties of the adhesive.

determined to be 0.45 ± 0.05mm. Finally, the unloading slope of the traction-separation curve was obtained by varying it until the numerical and experimental curves approximately matched after the peak load. Examples of the matching procedure is shown in Fig. 18. In the case being used as an example, the unloading slope was determined to be 40 MPa/mm. Upon completing these calculations it was noted that complete unloading of the traction-separation law at the original crack-tip had not occurred by the time the crack tip had run into the compressive region associated with the loading points. Even so, the total energy dissipated by the frictional portion of the traction-separation law was 5 ± 1 kJ/m^2 - a substantial addition to the cohesive energy associated with mode-II fracture.

This process of analysis was then repeated for all the individual sets of experimental data, with uncertainties in the cohesive parameters being computed for each rate. A summary of the cohesive strength and the mode-II toughness, and frictional are provided in Figs. 19 and 20 as functions of the crack velocity.

3.2 Numerical simulations for the clamped ENF geometry

The numerical model for the clamped ENF geometry was similar to that of the three-point-bending ENF geometry except for a clamped boundary condition. It is recognized that this clamping was an approximation, since observations indicated that there was sliding and rotation of the specimen in the clamp during impact. The continuum numerical calculations indicated that the strain rate of the adherends was about 2 /s at the clamped boundary when the velocity of the loading point was 600 mm/s (corresponding to a drop height of 30mm), and increased to 14 /s at the fastest velocities. Therefore, the constitutive properties of the steel were taken to be the upper bounds of the

properties reported in Sun *et al*. [2008a]. These same continuum calculations were also used to relate the shear strain rate in the adhesive layer to the loading rate. It was determined that the strain rate at the crack tip was in the range of 30 /s to 400 /s during the drop-dower tests, compared with 0.01 /s to 20 /s during the tests conducted with the servo-hydraulic machine .

As discussed in Section 2.2, the effects of rate in these clamped-ENF studies were manifested by two different types of deformation. Figure 13 shows a plastic hinge formed at the clamped root in a specimen loaded slowly, and a plastic hinge formed at the crack tip in a specimens loaded quickly. Continuum numerical calculations of the clamped ENF geometry indicated that the locations of the plastic hinge depended on the shear strength of the adhesive. In particular, the hinge formed at the crack tip when the shear strength was greater than 32 ± 3 MPa. Experimentally, it was observed that the hinge formed at this location at strain rates greater than between 20 /s and 30 /s, we can deduce that the maximum shear strength of the adhesive layer was greater than 29 MPa at strain rates above 30 /s and less than 35 MPa for strain rates below 20 /s.

The cohesive parameters at high loading rates were deduced from comparisons between the numerical and experimental results for the clamped ENF tests in the drop tower. No further effects of rate were observed from the load-displacement traces obtained at any of these high rates - specimen-to-specimen variations dominated any other effect. Therefore, a single set of high-rate mode-II parameters was obtained. Extrapolation of the uniaxial data from Sun *et al.* [2008a] to the strain rates appropriate for the drop- tower tests indicated that the shear modulus of the adhesive layer was about

350-500 MPa,. This corresponds to an initial slope for the traction-separation law of 440-625 MPa/mm.[6]

The cohesive shear strength was determined from the second portion of the experimental load-displacement curves, after the deviation from linearity induced by the plastic flow of the adhesive and steel. (While this region may not be particularly obvious in Fig. 10, a difference in the shapes of the numerical curves could be detected as the parameters were changed.) Fits to the numerical curves suggested that the mode-II cohesive strength was in the range of 25 MPa to 50 MPa. However, it should be noted that, as discussed above, the location of the plastic hinge at the crack tip imposes a more limiting lower-bound of 32 ± 3 MPa for the shear cohesive strength at the loading rates obtained in the drop-tower tests. So, for consistency, the shear cohesive strength at strain rates above to be between 29 MPa and 50 MPa for strain rates above 30 /s.

The displacement at which unloading of the traction-separation law begins was determined to be 0.25 ± 0.05 mm. This was done by matching the peak loads of the numerical and experimental load-displacement plots (Fig. 9). The unloading slope of the traction-separation law was determined to be 25-50 MPa/mm. This was done by matching the shapes of the numerical and experimental load-displacement curves after the peak load. The critical displacement at which the crack began to grow was determined to be 0.8 ± 0.2 mm, which corresponds to a mode-II toughness of 17 ± 5 kJ/m^2. This was done by matching the points on the load-displacement curves at

[6] Use of this range in the numerical analysis for the clamped ENF geometry resulted in load-displacement predictions that were much too stiff, because the numerical boundary conditions simulations were too restrictive compared with the experimental clamping. Owing to the difficulty in correctly modeling the boundary conditions, the additional compliance associated with slipping at the clamp was incorporated into the initial slope (225 MPa/mm) of the mode-II cohesive law while analyzing this geometry.

which crack growth was seen during the experiments to the point at which crack growth began in the numerical calculations. The remainder of the cohesive law, after crack propagation was associated with frictional dissipation of 5 ± 4 kJ/m^2. It will be noted that the clamped configuration of the ENF geometry resulted in crack growth beginning *after* the peak load; this is in contrast to the simply-supported geometry in which crack growth began *before* the peak load. This a difference in behavior that is associated with the relatively large deformations and the different boundary conditions.

Figure 21 shows the results of the numerical simulation after this cohesive law had been developed, and compares the results to the experimental observations from the drop-tower results. The values for the cohesive parameters used for these high-rate simulations have been added to Figs. 19 and 20. The deformed shape of the clamped, ENF geometry using these high-rate parameters is shown in Fig. 22(a). It will be noted that the plastic hinge was formed at the initial crack tip, as seen experimentally. Furthermore, using a mode-II cohesive law appropriate to the rates that can be obtained with the servo-hydraulic machine, the plastic hinge was formed at the root of the beam, where the specimen is clamped. The result of this simulation is shown in Fig. 22(b). This difference in behavior is consistent with experimental observations illustrated in Fig. 12.

3.3 Numerical simulations for the lap-shear geometry

A numerical analysis with continuum elements (plane strain) representing the adhesive layer indicated that the displacement rates during the lap-shear tests corresponded to shear-strain rates in the adhesive of between 0.013 s^{-1} and 250 s^{-1}. A final set of numerical calculations were performed using the cohesive-zone model for the

lap-shear test. These calculations confirmed that for this geometry and combination of materials, the nominal shear strength of the bond was identically equal to the cohesive shear strength. The values for mode-II cohesive strengths obtained from the lap-shear tests have been added to Fig. 19.

4. CONCLUSIONS

Stick-slip behavior was not observed during mode-II deformation in this adhesive system. This is a significant contrast to the mode-I observations for the same system, in which random transitions to an untoughened mode of fracture was observed [Sun *et al.*, 2008a]. Crack propagation was interfacial in mode-II for this system; mode-II crack growth within the adhesive layer was not observed. Again, this is in contrast to the behavior in mode-I where the crack appeared to be stabilized within the adhesive layer in this system.

Cohesive-zone analyses of the data showed that the fracture parameters were slightly rate sensitive. As indicated in Figs. 20 and 21, this rate sensitivity was very slight and not very significant beyond the range of experimental uncertainty; it resulted in only one unambiguous rate effect within the entire range of rates studied - a change in the location of the plastic hinge during the clamped ENF studies. The mode-II toughness ranged from about 8 kJ/m^2 to about 21 kJ/m^2 (including uncertainties) at crack velocities between 0.4 mm/s and 2400 mm/s for this adhesive. While the toughness appears to have increased slightly with rate, any increase was within the range of uncertainty. In a similar fashion, the mode-II cohesive strength was between 20 to 45 MPa, with any increase with rate being small compared to the level of uncertainty.

ACKNOWLEDGEMENTS

C. Sun, M. D. Thouless and A. M. Waas gratefully acknowledge the financial support of General Motors.

APPENDIX

The mixed-mode cohesive-zone model used in this study is based on that described in Yang and Thouless [2001] and Li *et al.* [2006]. The mode-I and mode-II traction-separation laws are uncoupled in the sense that each law can be described separately, with the parameters for each law being determined by either mode-I or mode-II experiments. During numerical analyses, the energy-release rate for each mode is calculated independently by integration of the opening and shear traction-separation laws (Fig. A1)

$$\mathcal{G}_I = \int_0^{\delta_n} \sigma(\delta_n) d\delta_n ; \qquad \mathcal{G}_{II} = \int_0^{\delta_t} \tau(\delta_t) d\delta_t , \tag{A1}$$

where δ_n and δ_t denote the relative normal and shear displacements. Coupling between the two modes is provided by the mixed-mode failure criterion. An example of a simple mixed-mode failure criterion is given by

$$\mathcal{G}_I / \Gamma_I + \mathcal{G}_{II} / \Gamma_{II} = 1, \tag{A2}$$

where Γ_I and Γ_{II} are the total areas under the curves (integration up to the critical displacements δ_{nc} and δ_{tc}). In the cohesive-zone analyses, $\mathcal{G}_I$ and $\mathcal{G}_{II}$ are evaluated independently for each element. The element is assumed to fail when the mixed-mode failure criterion is met, and the crack advances by one element. This approach results in a very robust agreement with mixed-mode LEFM models under appropriate linear-elastic conditions [Parmigiani and Thouless, 2007]. It also provides good predictive capabilities for mixed-mode problems when LEFM is not applicable [Yang and Thouless, 2001; Li *et al.* 2006].

The mixed-mode cohesive-zone model described above appears to be an excellent numerical tool for adhesively-bonded structures in which the adhesive layer is significantly thinner than the adherends. Under these conditions, failure to capture accurately the coupling between the shear and normal deformations of the adhesive is not important, because deformation of the adhesive before fracture does not contribute significantly to the overall behavior of the system. However, when the adhesive layer is relatively thick compared to the adherends (as in the present study), then an accurate description of the coupling between the shear and normal modes of deformation becomes important, as the adhesive has a significant effect on the overall behavior of the system even before it fails. It is this issue that the modified coupled-cohesive-zone model (CCZM) described below addresses.

To illustrate the problem discussed above, the uncoupled cohesive-zone model was used in a numerical model of the ENF test at a displacement rate of 0.1 mm/s. The adhesive layer bonding the steel coupons together was replaced by four-node cohesive-zone elements with an initial thickness of 0.8 mm. The mode-II cohesive parameters were chosen to mimic the shear stress-strain curve of the adhesive given in Fig. 16. As shown in Fig. A2, the uncoupled cohesive-zone model could not match the experimental results or continuum calculations. In particular, the cohesive-zone model did not correctly capture the deformation of the specimen *before* fracture. This implies that the cohesive elements, which represented the adhesive layer, were not mimicking the deformations of the adhesive layer correctly; the problem was independent of the choices made for the cohesive parameters. The stiffness for the mode-II law was not the cause for this discrepancy - the initial slopes of the load-deflection curves all match. The error

associated with the cohesive-zone analysis becomes more pronounced as the strains increased.

The poor modeling capacity of the uncoupled mixed-mode cohesive-zone model seen in Fig. A2 between the results of the uncoupled mixed-mode cohesive-zone model, and either the experimental results or the continuum model arises from the moments that develop across a cohesive-zone element when there is extensive shear deformation. In uncoupled cohesive-zone elements, the reaction forces on the nodes, F_y and F_x, arise only from the mode-I and mode-II displacements, as described by the separate mode-I and mode-II traction-separation laws (Fig. A3). However, these reaction forces induce a moment M under the effect of shear deformation. This moment can be significant if the shear displacements are large. If they are neglected in the formulation of the element, this moment equilibrium is violated. This can be neglected if the shear strains are small, or if the adhesive layer is thin compared to the thickness of the specimen. However, as seen in Fig. A2, the geometry and deformation in the present case are such that this deficiency has a significant effect on the overall behavior of the system.

A modified cohesive-zone element was formulated that we refer to as a coupled cohesive-zone element (CCZM) to eliminate the inaccuracies associated with this unbalanced moment. Fig. A3a shows an element of length (along the interface) L_e and height (perpendicular to the interface) T_e. The element is deformed to a new length L_{ed} and height T_{ed} (Fig. A.3b). The top and bottom surfaces of the element are sheared relative to each other by D_x. The total moment on the element that is associated with the normal nodal reaction forces is equal to $2F_y \cdot D_x$. This moment can be eliminated by applying a couple force, $F_{yx} = F_y \cdot D_x / L_{ed}$, to each node, as shown in Fig. A3c. There is

also a moment induced by the shear nodal reaction forces of $2F_x \bullet T_{ed}$ This moment can be eliminated by applying a couple force, $F_{xy} = F_x \bullet T_{ed} / L_{ed}$, to each node, as shown in Fig. A3d. This modification to the formulation of the cohesive elements eliminates the effects of the moment and couples the shear and normal tractions, without affecting the cohesive parameters. An example of the code given in Sun [2007]. Simulation of the ENF geometry using these coupled elements, but using the *same* cohesive parameters as for the earlier analysis of Fig. A2 are shown in Fig. A4. Now, it will be observed that the cohesive-zone model provides good agreement with the continuum results.

Finally, to verify that the results of the two types of cohesive models are essentially identical when the adhesive layer is thin enough to avoid the complications discussed above, a similar ENF geometry with thicker arms was analyzed. Both types of cohesive-zone model were used, both with identical tractions-separation laws, but with much thicker adherends (the steel arms was increased by a factor of 3 to 4.2 mm). All other dimensions and properties were identical to those used in Fig. A2. Now, as shown in Fig. A.5, both models are in agreement with the continuum model, showing that the effect discussed in this Appendix is independent of the choice of cohesive parameters and is significant only when there are relatively large shear deformations.

REFERENCES

Barrett, J. D., and R. O. Foschi [1977]. "Mode II stress-intensity factors for cracked wood beams," *Engineering Fracture Mechanics,* **9**, 371-378.

Blackman, B. R. K., A. J. Kinloch and M. Paraschi [2006]. "The determination of the mode II adhesive fracture resistance, G_{IIC}, of structure adhesive joints: an effective crack length," *Engineering Fracture Mechanics*, **72**, 877-897.

Bulchholz, F. G., R. Rikards and H. Wang [1997]. "Computational analysis of interlaminar fracture of laminated composites," *International Journal of Fracture*, **86**, 37-57.

Caimmi, F., R. Frassine and A. Pavan [2006]. "A new jig for mode II interlaminar fracture testing of composite materials under quasi-static and moderately high rate of loading," *Engineering Fracture Mechanics*, **73**, 2277-2291.

Carlsson, L. A., J. W. Gillespie and R. B. Pipes [1986]. "On the analysis and design of the end notched flexure specimen for mode II testing," *Journal of Composite Materials*, **20**, 594-603.

Chai, H. [1988]. "Shear Fracture," *International Journal of Fracture*, **37**, 137-159.

Edde, F. C., and Y. Verreman [1995]. "Nominally constant strain energy release rate specimen for the study of mode II fracture and fatigue in adhesively bonded joints," *International Journal for Adhesion and Adhesives*, **15**, 29-32

Giambanco, G., and G. F. Scimemi [2006]. "Mixed mode failure analysis of bonded joints with rate-dependent interface models," *International Journal for Numerical Methods in Engineering*, 67,1160-1192

Jacob, G. C., J. M. Starbuck, J. F. Fellers, S. Simunovic and R. G. Boeman [2005]. "The effect of loading rate on the fracture toughness of fiber reinforced polymer composites," *Journal of Applied Polymer Science,* **96**, 899-904.

Leffler, K., K. S. Alfredsson and U. Stigh [2007]. "Shear behaviour of adhesive layers," *International Journal of Solids and Structures*, **44**, 530-545.

Li, S., M. D. Thouless, A. M. Waas, J. A. Schroeder and P. D. Zavattieri [2006]. "Mixed-mode cohesive-zone models for fracture of an adhesively-bonded polymer-matrix composite," *Engineering Fracture Mechanics*, **73**, 64-78.

Liechti, K.M., and J. Wu [2001]. "Mixed-mode, time-dependent rubber/metal debonding," *Journal of the Mechanics and Physics of Solids*, **49**, 1039–1072.

Parmigiani J. P. and M. D. Thouless [2007]. "The Effects of Cohesive Strength and Toughness on Mixed-mode Delamination of Beam-Like Geometries," *Engineering Fracture Mechanics,* **74**, 2675-2699.

Qiao, P., J. Wang and J. F. Davalos [2003]. "Analysis of tapered ENF specimen and characterization of bonded interface fracture under mode II loading," *International Journal of Solids and Structure*, **40**, 1865-1884.

Sun, C. [2007]. "Fracture of plastically-deforming, adhesively-bonded structures: experimental and numerical Studies," Ph.D. dissertation, University of Michigan, Ann Arbor, MI.

Sun, C., M. D. Thouless, A. M. Waas, J. A. Schroeder and P. D. Zavattieri [2008a]. "Ductile-brittle transitions in the fracture of plastically-deforming, adhesively-bonded structures: I experimental studies," *International Journal of Solids and Structures*, **45**, 3059-3073.

Sun, C., M. D. Thouless, A. M. Waas, J. A. Schroeder and P. D. Zavattieri [2008b]. "Ductile-brittle transitions in the fracture of plastically-deforming, adhesively-bonded structures: II numerical studies," *International Journal of Solids and Structures*, **45**, 4725-4738.

Sun, C., M. D. Thouless, A. M. Waas, J. A. Schroeder and P. D. Zavattieri [2008c]. "Rate effects for mixed-mode fracture of plastically-deforming, adhesively-bonded structures," *International Journal of Adhesion and Adhesives* (in press).

Sun, X., and B. D. Davidson [2006]. "Numerical evaluation of the effects of friction and geometric nonlinearities on the energy release rate in three- and four-point bend end-notched flexure tests," *Engineering Fracture Mechanics*, **73**, 1343-1361.

Tvergaard, V., and J. W. Hutchinson [1992]. "The relation between crack-growth resistance and fracture process parameters in elastic plastic solids," *Journal of the Mechanics and Physics of Solids*, **40**, 1377–1397.

Ungsuwarungsri, T. and Knauss, W. G. [1987]. "Role of damage-softened material behavior in the fracture of composites and adhesives," International Journal of Fracture, **35**, 221–41.

Yang, Q. D., M. D. Thouless and S. M. Ward [1999]. "Numerical simulations of adhesively bonded beams failing with extensive plastic deformation," *Journal of the Mechanics and Physics of Solids*, **47**, 1337–1353.

Yang, Q. D, M. D. Thouless and S. M. Ward [2001]. "Elastic-plastic mode-II fracture of adhesive joints," *International Journal of Solids and Structure*, **38**, 3251-3262.

Yang, Q. D., and M. D. Thouless [2001]. "Mixed-mode fracture analyses of plastically-deforming adhesive joints," *International Journal of Fracture*, **110**, 175-187.

Zhu, Y, K. M. Liechti and K. Ravi-Chandar [2009]. "Direct extraction of rate-dependent traction–separation laws for polyurea/steel interfaces," *International Journal of Solids and Structure*, **46**, 31-51.

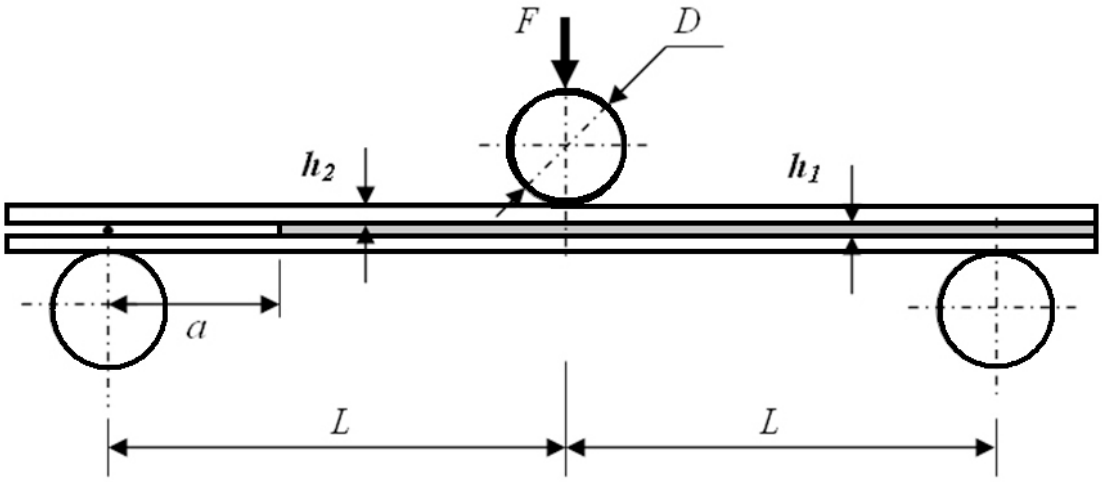

Figure 1 Configuration of the three-point bending, end-notched flexure (ENF) specimens. The thickness of the steel coupon is $h_2 = 1.42 \pm 0.02$ mm; the thickness of the adhesive is $h_1 = 0.8 \pm 0.1$ mm; the width is $W = 20.0 \pm 0.5$ mm; the initial crack length is $a = a_0 = 10 \pm 1$ mm; the half span is $L = 30 \pm 1$ mm; and the diameter of cylinders is $D = 12 \pm 0.5$ mm.

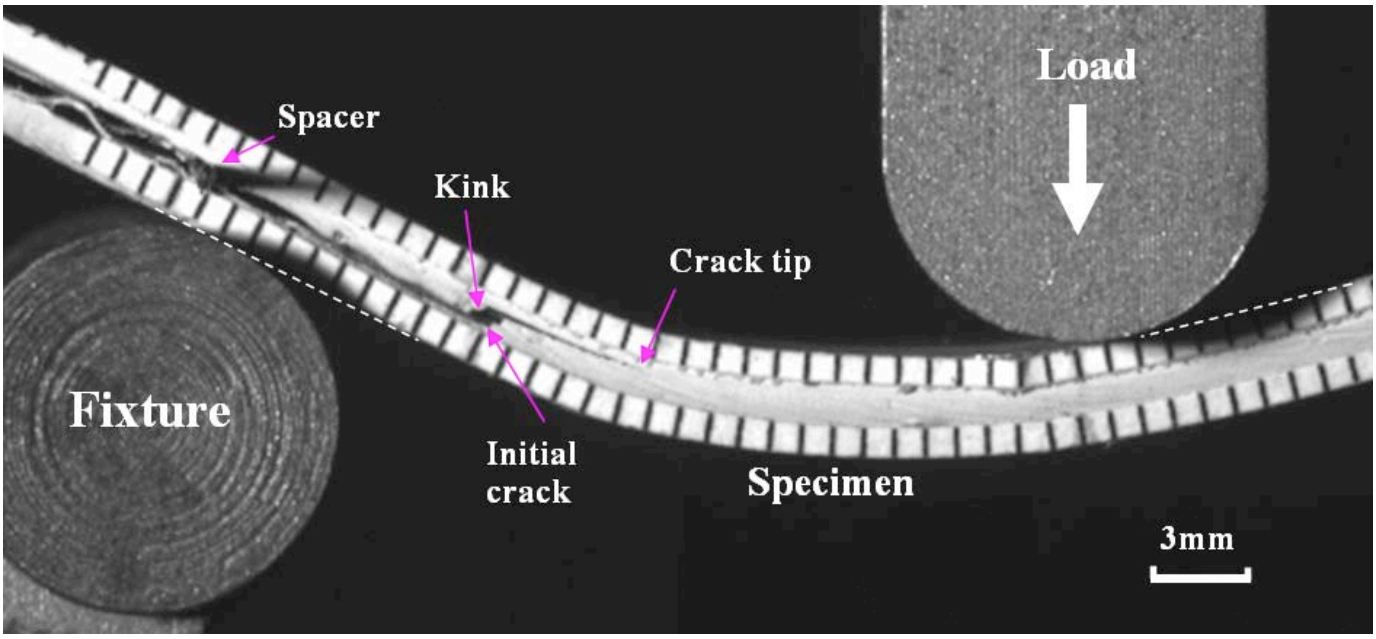

Figure 2 Micrograph of the experimental arrangement for the three-point bending ENF test. This image shows a crack that has kinked to the top interface.

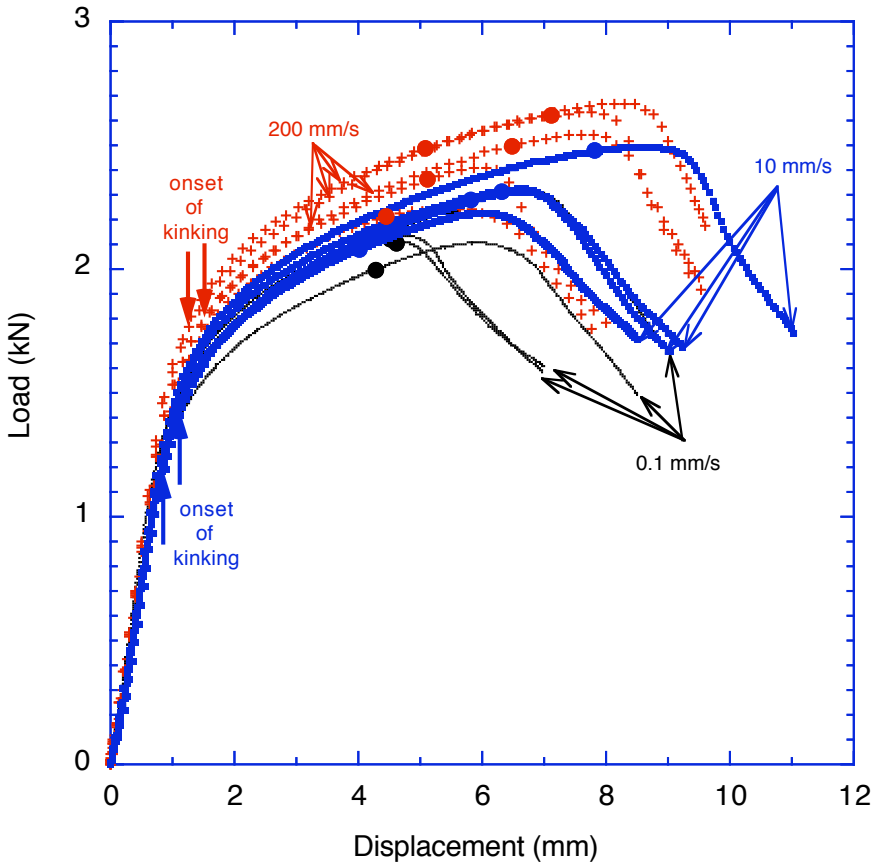

Figure 3 Load plotted against mid-point deflection for the ENF tests at three displacement rates (0.1 mm/s, 10mm/s and 200mm/s). The onset of kinking and crack propagation are marked by arrows and black dots respectively.

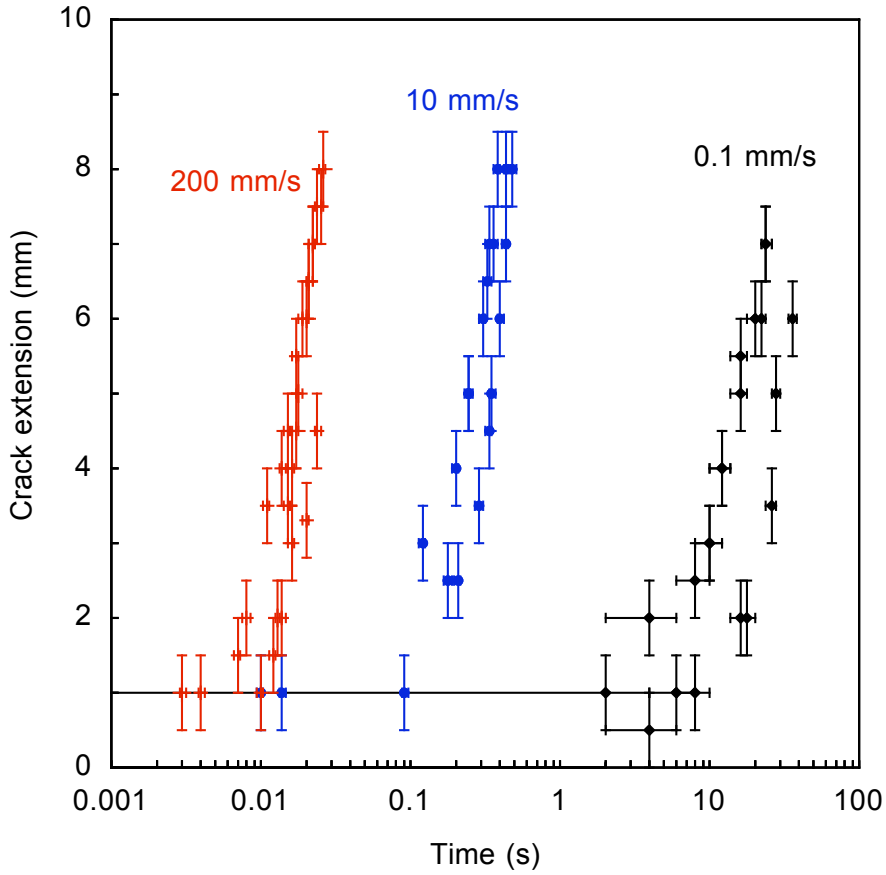

Figure 4 Crack extension plotted against time for the ENF tests at displacement rates of 0.1 mm/s, 10mm/s and 200mm/s.

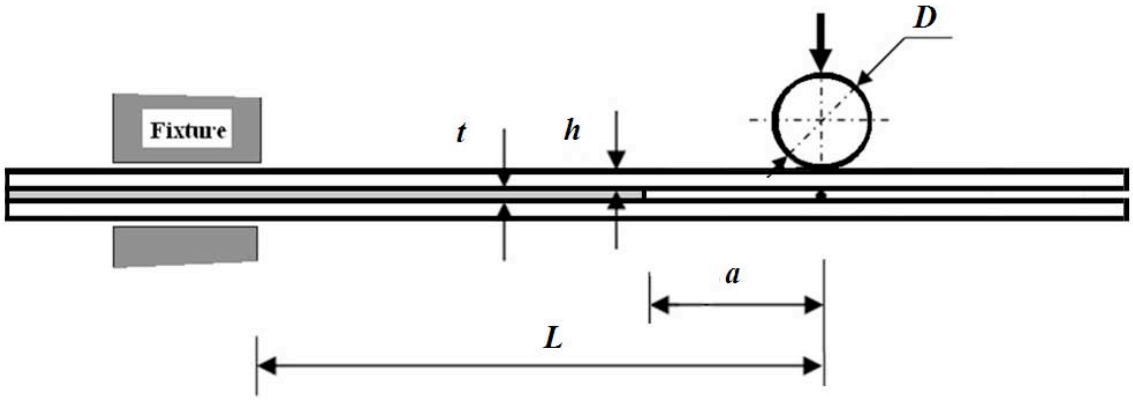

Figure 5 Configuration of the clamped, end-notched flexure (ENF) specimens. The thickness of the steel coupon is $h_2 = 1.42 \pm 0.02$ mm; the thickness of the adhesive is $h_1 = 0.8 \pm 0.1$ mm; the width is $W = 20.0 \pm 0.5$ mm; the initial crack length is $a = a_0 = 10 \pm 1$ mm; the distance between the clamp and loading point is $L = 30 \pm 1$ mm; and the diameter of cylinders is $D = 12 \pm 0.5$ mm.

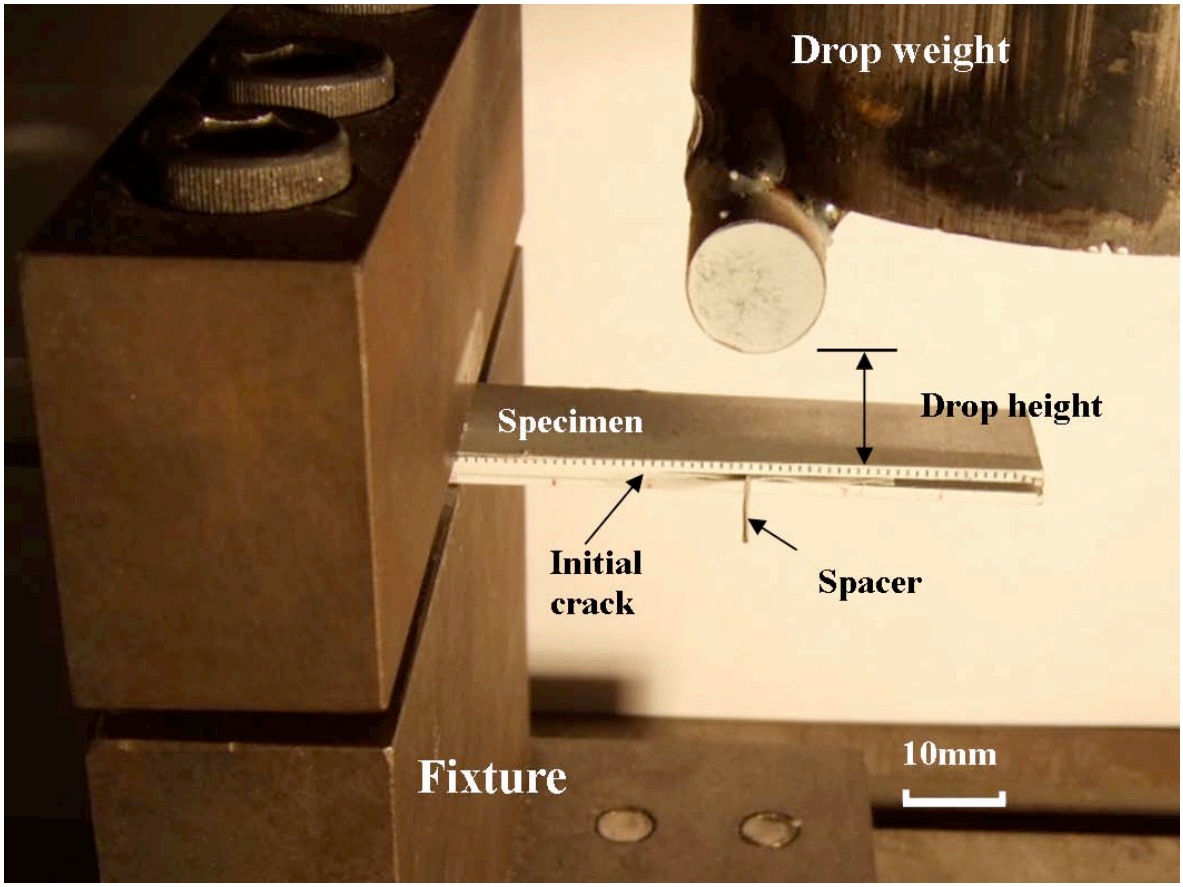

Figure 6 Micrograph of the experimental setup for a clamped, ENF test. The specimen is clamped between two blocks of steel in this fixture by means of four screws.

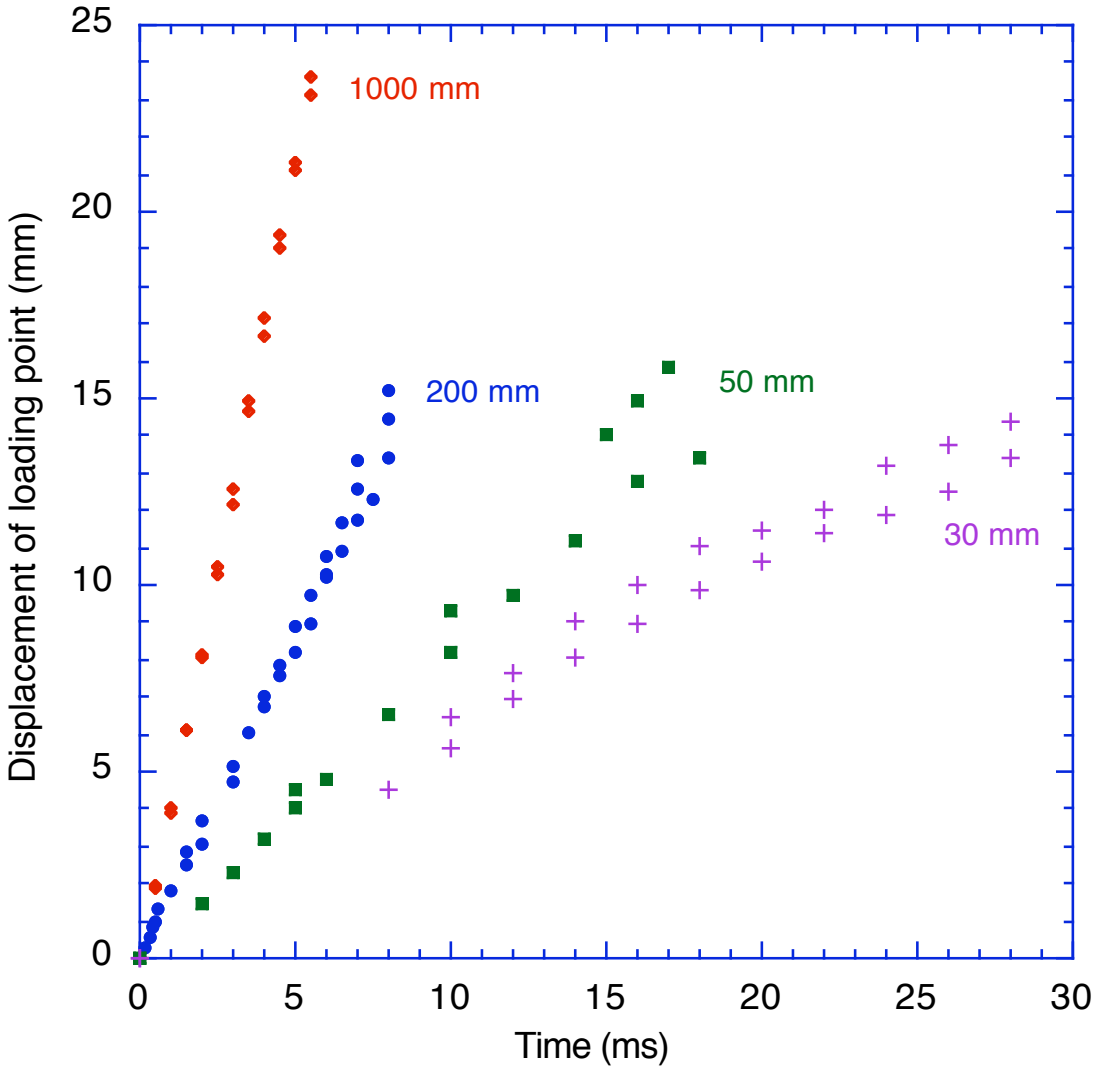

Figure 7 Displacement of the loading point plotted against time for the clamped, ENF tests with drop height of 30 mm, 50mm, 200mm and 1000mm. The velocity of the loading point was 900 ± 50 mm/s, 1800 ± 100 mm/s and 4200 ± 50 mm/s for the last three conditions, and varied from about 300 to 600 mm/s for the lowest drop height.

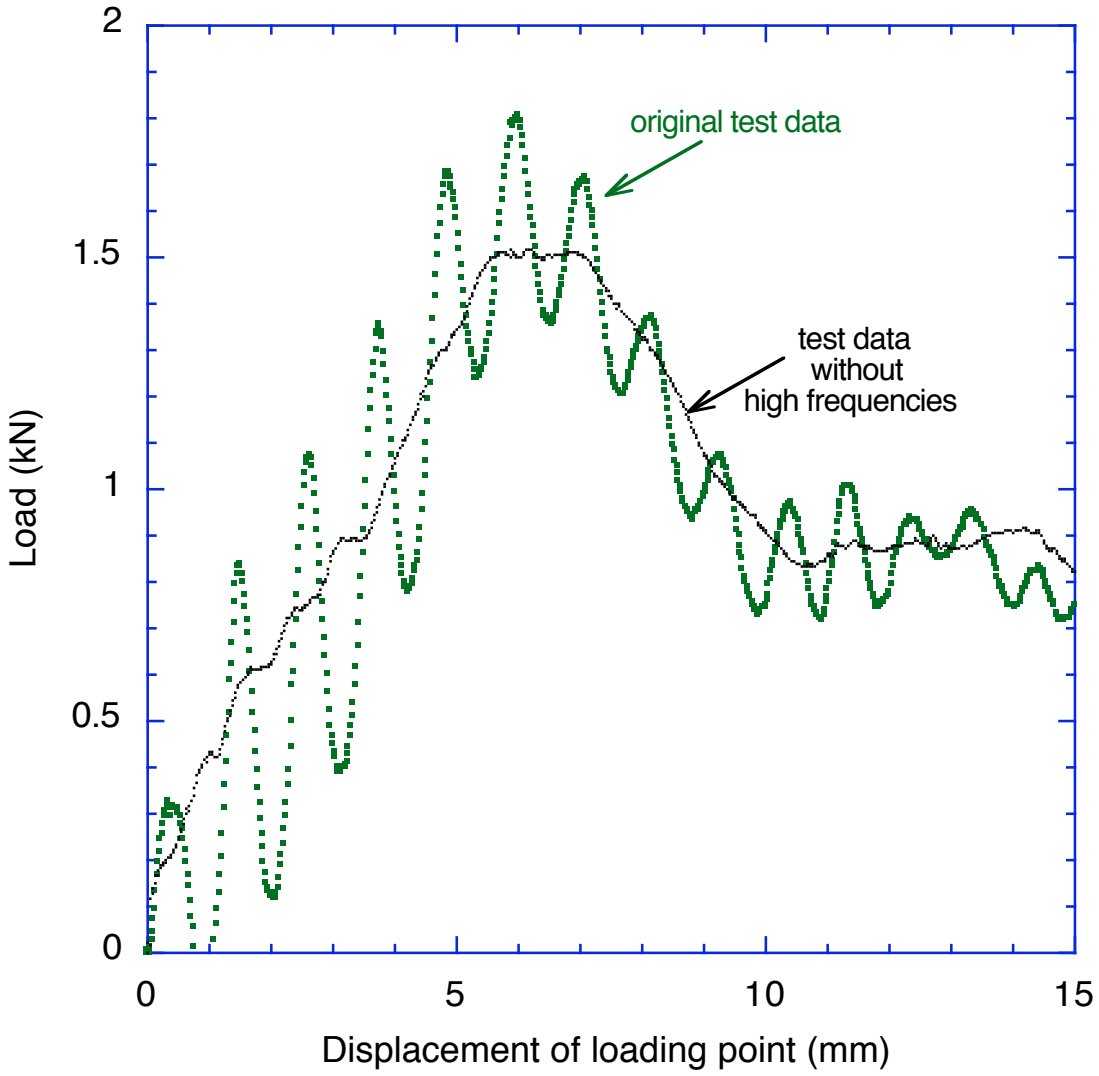

Figure 8 A typical plot of load against end deflection for the clamped, ENF tests with a drop height of 200 mm. The curve was smoothed by digital filtering using a discrete Fourier transform.

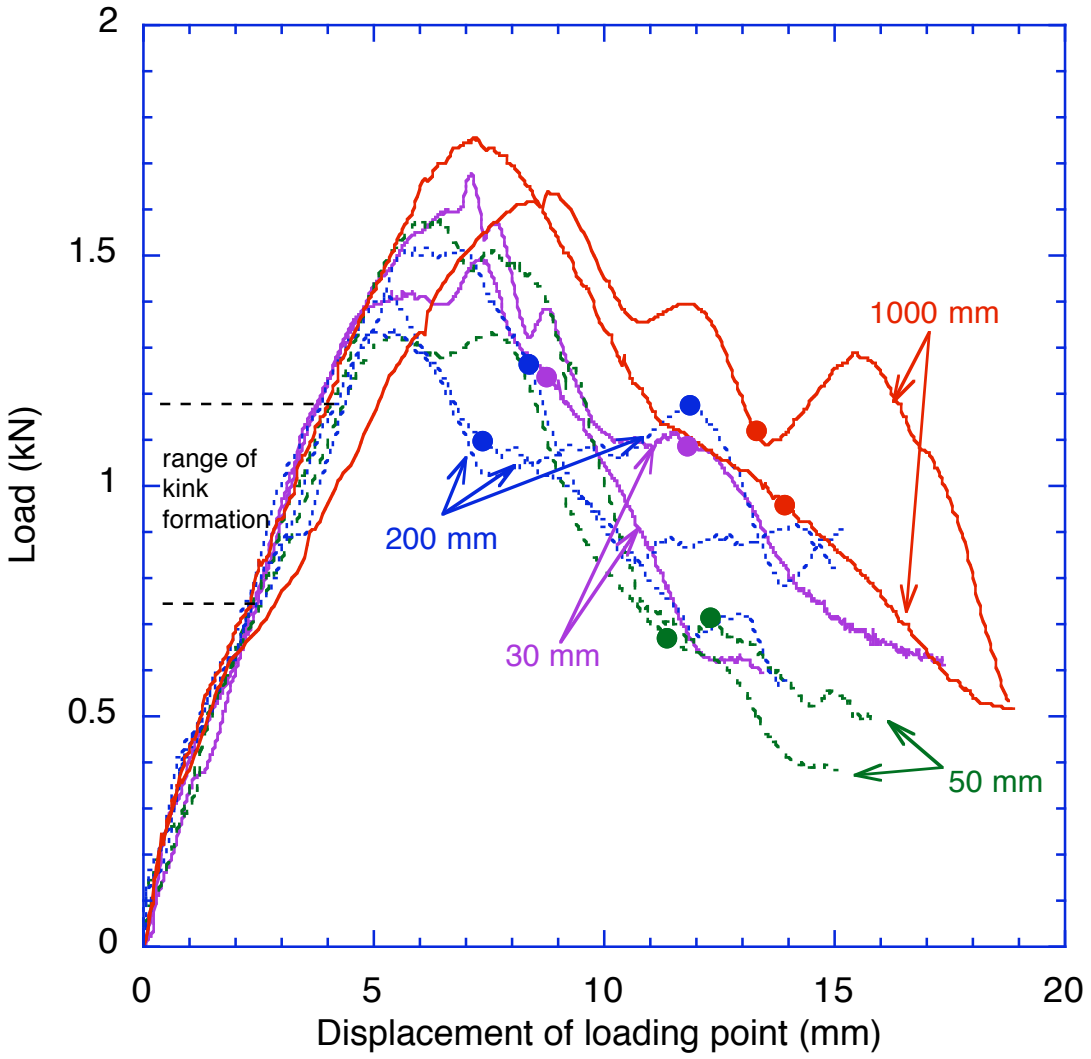

Figure 9 Summary of the loads plotted against load point deflections for the clamped, ENF tests with drop height of 10mm, 30 mm, 50mm, 200mm and 1000mm. The differences in the load-displacement plots do not appear to be correlated with displacement rates, and are probably associated with minor differences in the specimen geometry and clamping conditions. The onsets of kinking and crack propagation are marked by arrows and black dots respectively. The initial crack position is 10.7 ± 2.2 mm for all the tests.

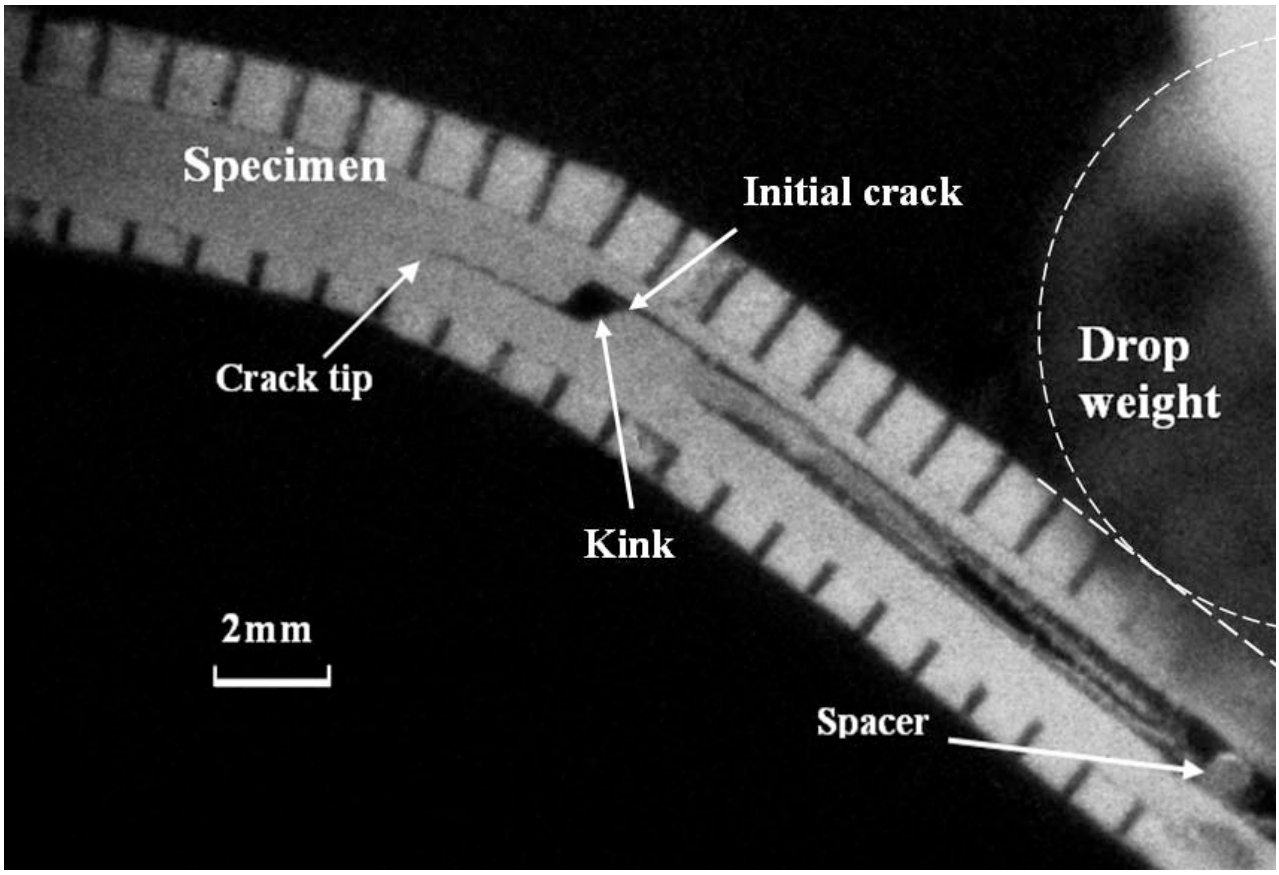

Figure 10 Micrograph of a deformed clamped, ENF specimen during the drop-tower test with a drop height of 30 mm.

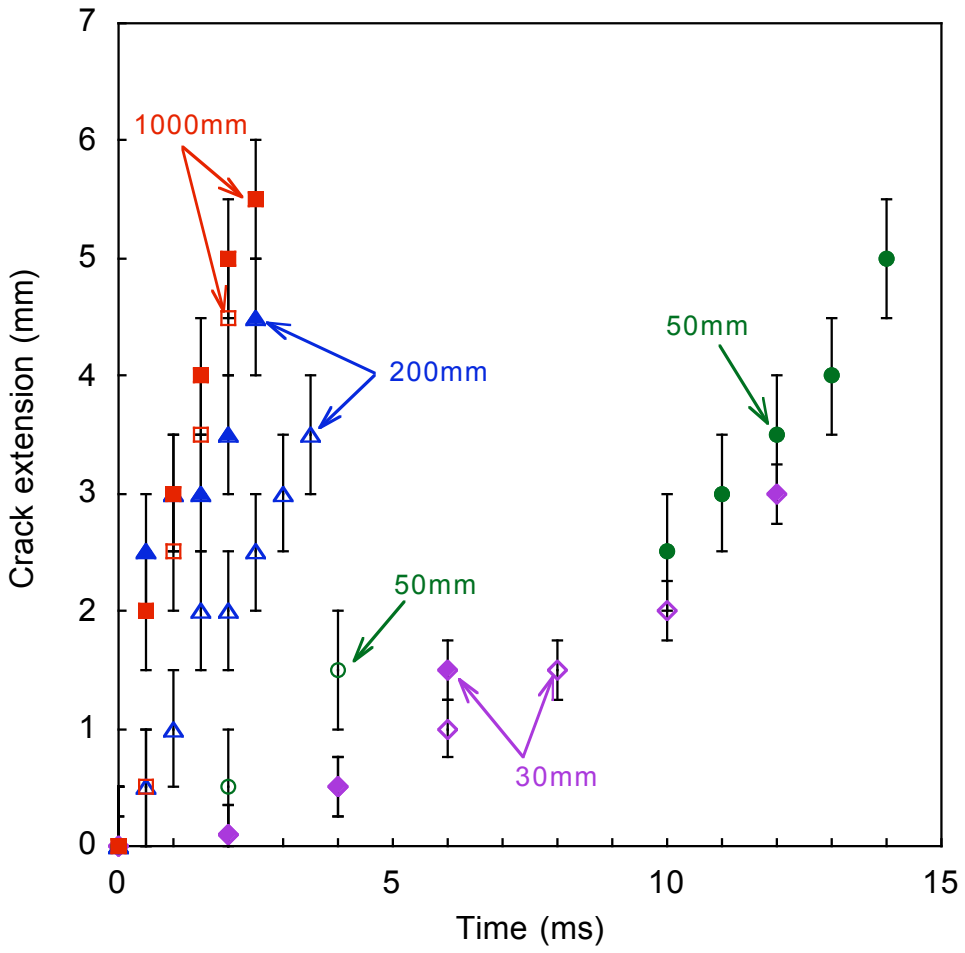

Figure 11 Crack extensions as a function of time for the clamped, ENF specimens with different drop heights.

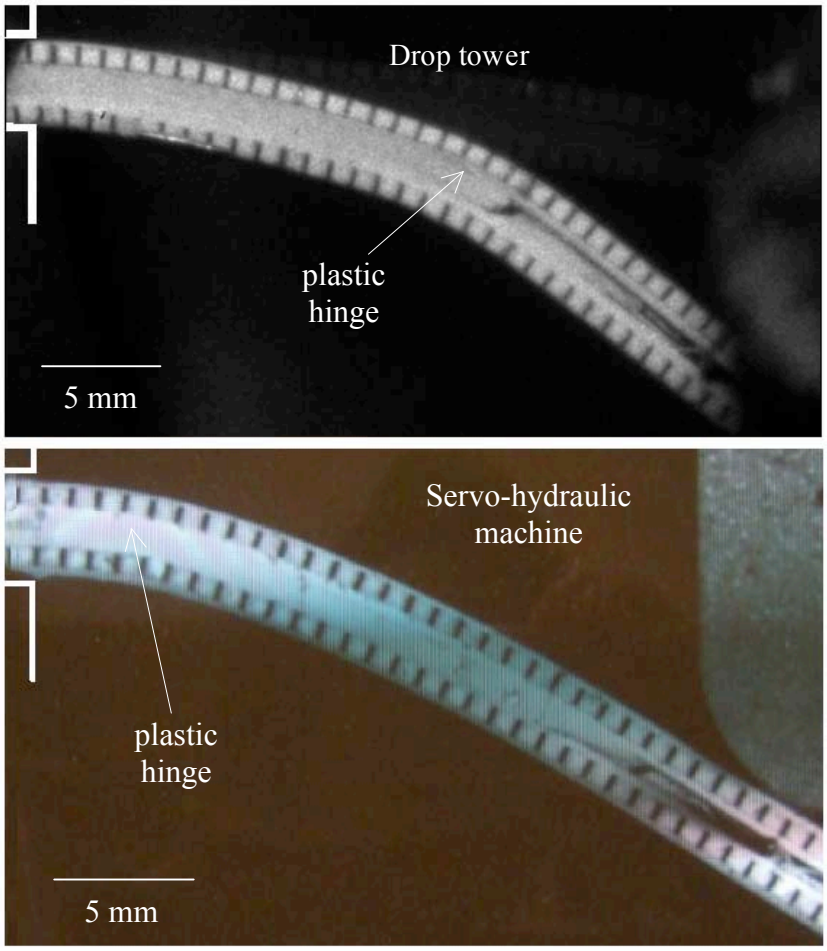

Figure 12 A comparison between the deformed shape of the clamped ENF specimens on **(a)** the drop-tower machine with a drop height of 200mm (corresponding to a displacement rate of 1800mm/s), and **(b)** the servo-hydraulic machine at a displacement rate of 0.1mm/s. The plastic hinge was formed near the crack tip for the drop-tower tests, and it formed near the clamped root of the specimen at the lower loading rates associated with the servo-hydraulic machine.

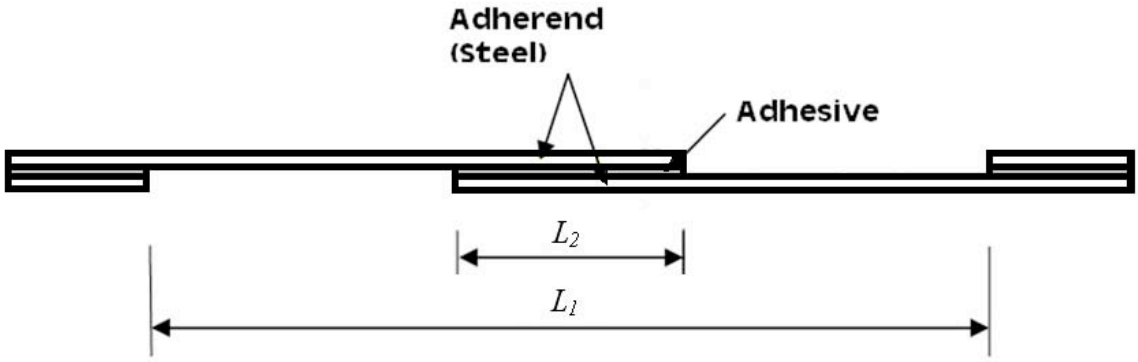

Figure 13 Geometry of the lap-shear test specimens used in this study. The free arm length is $L_1 = 80 \pm 2.0$ mm; the overlap length is $L_2 = 21.0 \pm 1.0$ mm; and the out-of-plane width is $W = 20.0 \pm 0.5$ mm.

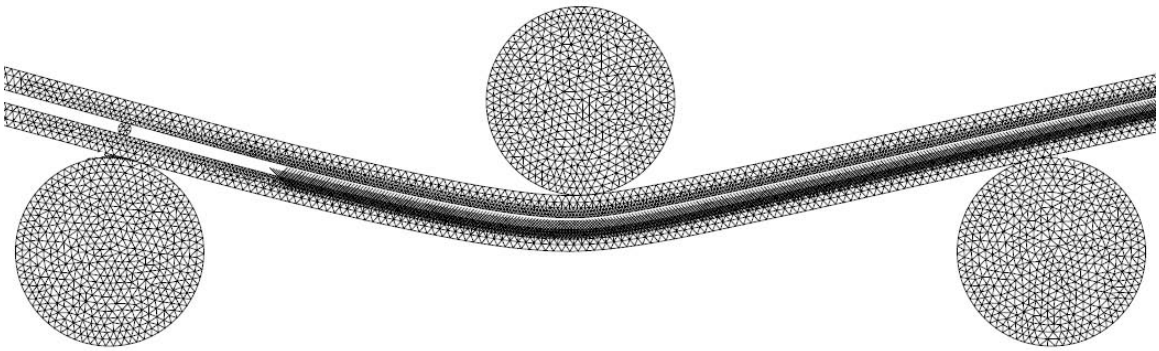

Figure 14 Geometry of the continuum/cohesive-zone model used to study the ENF tests. In the continuum model, the adhesive layer was replaced by plain-strain elements with initial thickness of 0.8 mm. In the cohesive-zone model, the adhesive layer was replaced by cohesive-zone elements with an initial thickness of 0.8 mm. The other dimensions are given in Fig. 1.

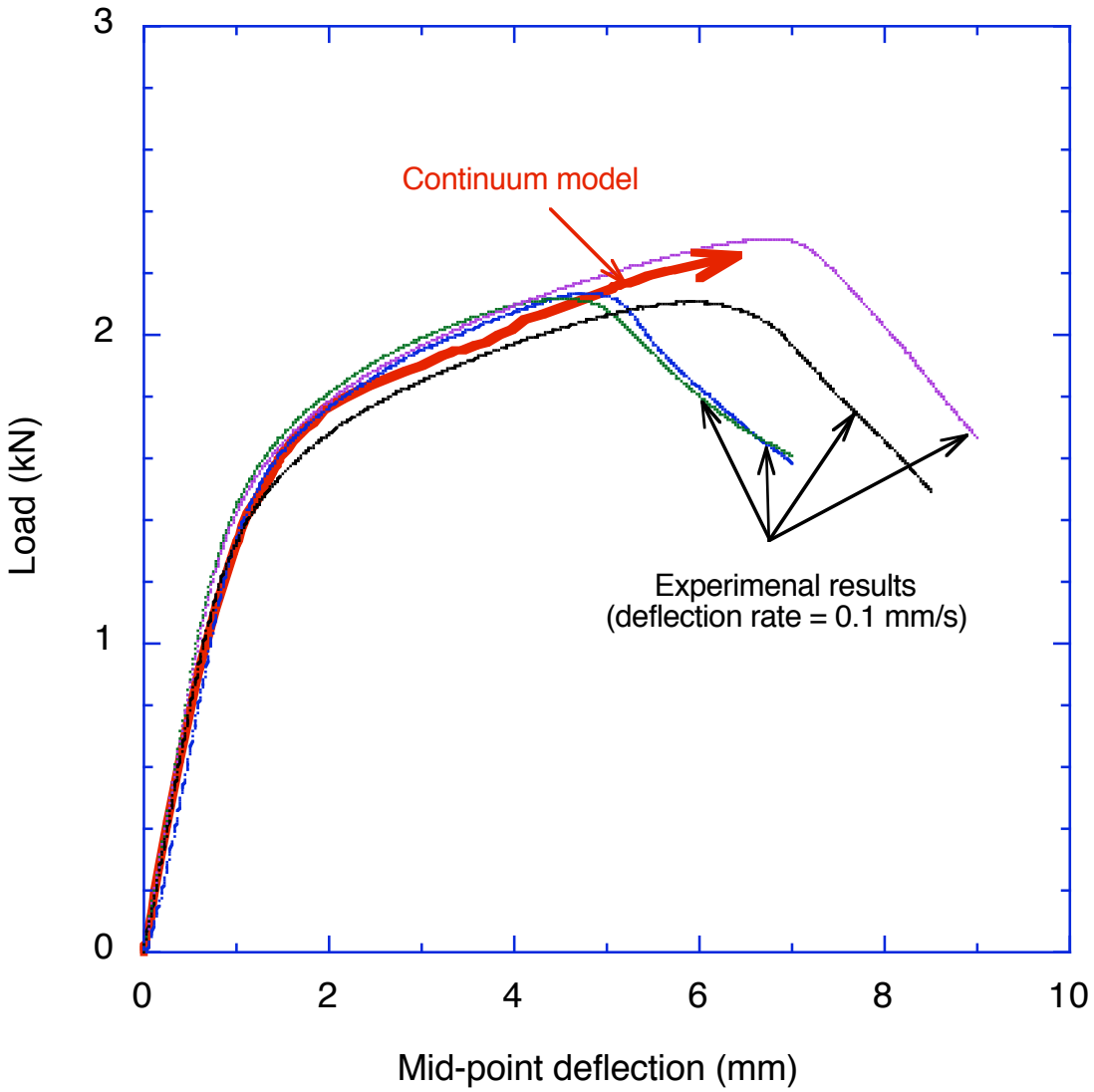

Figure 15 Comparison between the load-deflection plot obtained from an ENF test conducted at a deflection rate of 0.1 mm/s and the numerical predictions of a continuum model with the constitutive properties of the adhesive obtained from a tensile test (Sun *et al.* 2008a).

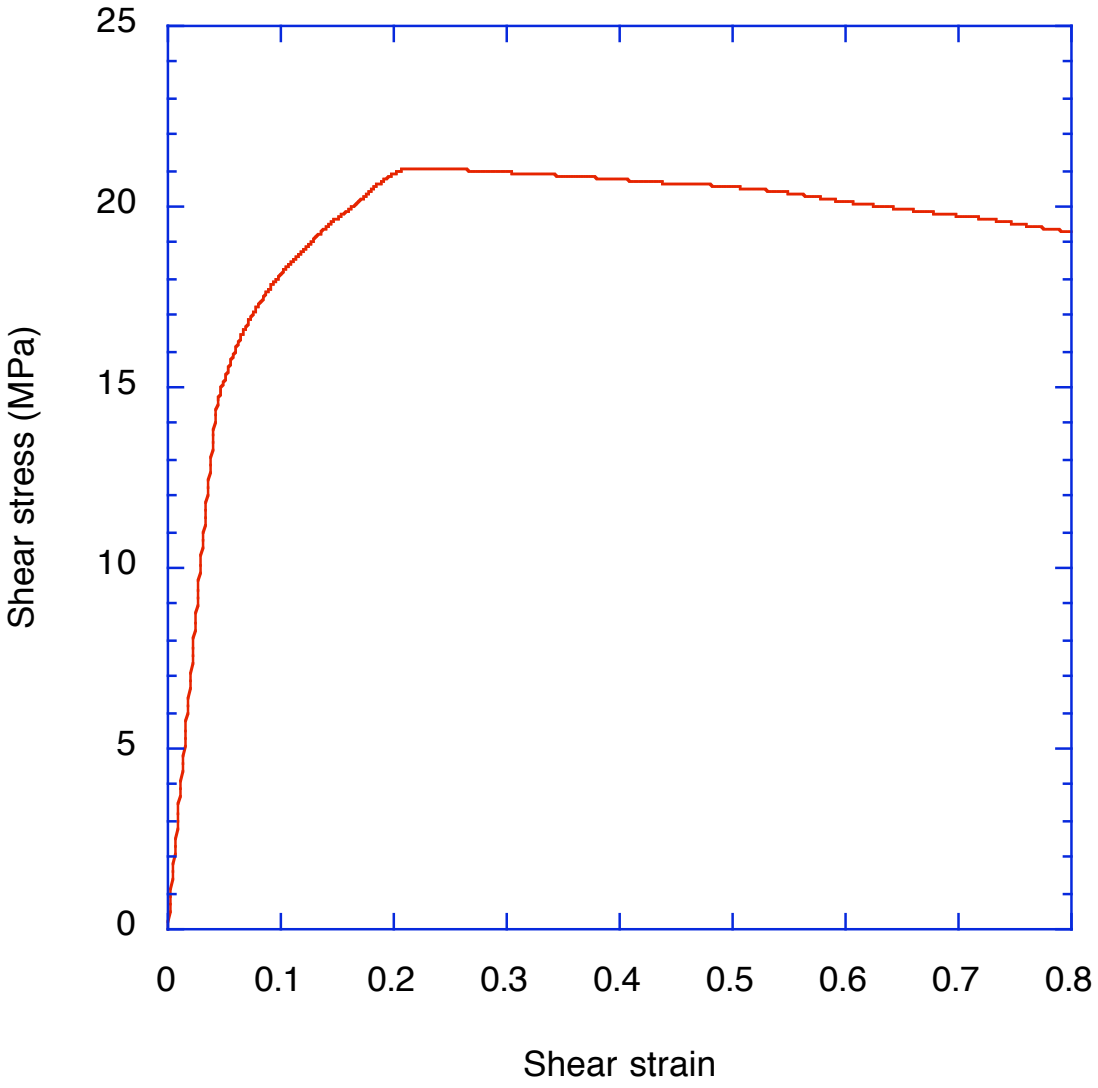

Figure 16 The relationship between shear stress and shear strain for an adhesive layer at a shear strain rate of about 0.0115 s^{-1}. This curve was derived from the stress-strain relationship of an element at the crack tip in the continuum analysis of the ENF test of Fig. 15.

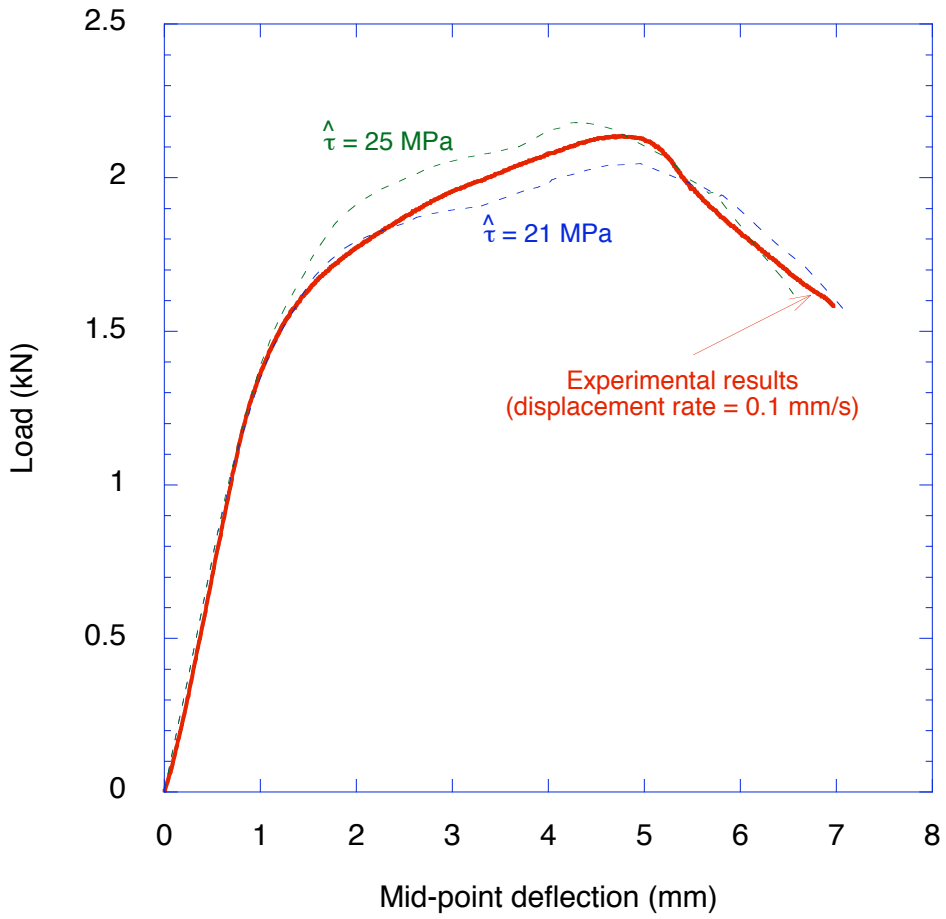

Figure 17 A comparison between the results of a cohesive-zone analysis and the numerical results for an ENF test at a displacement rate of 0.1 mm/s. The cohesive strength is determined by comparing the point at which the curves deviate from a linear load-deflection relationship.

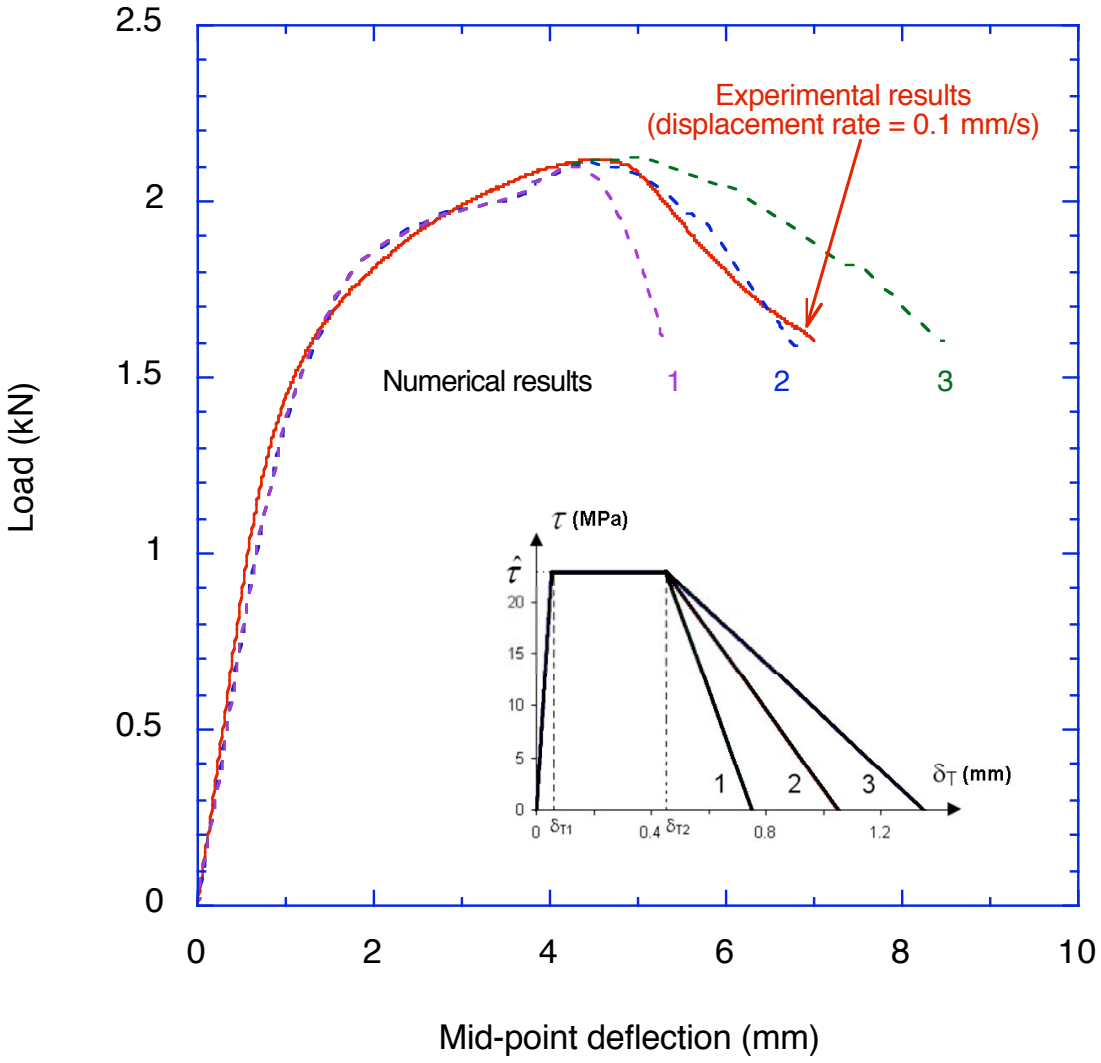

Figure 18 The unloading slope of the traction-separation law has fairly significant effects on the load-displacement curve. An estimate of the amount of energy dissipated by friction can be obtained by altering the unloading slope in the cohesive law, so that the unloading portion of the numerical load-deflection curve matches the experimental curve.

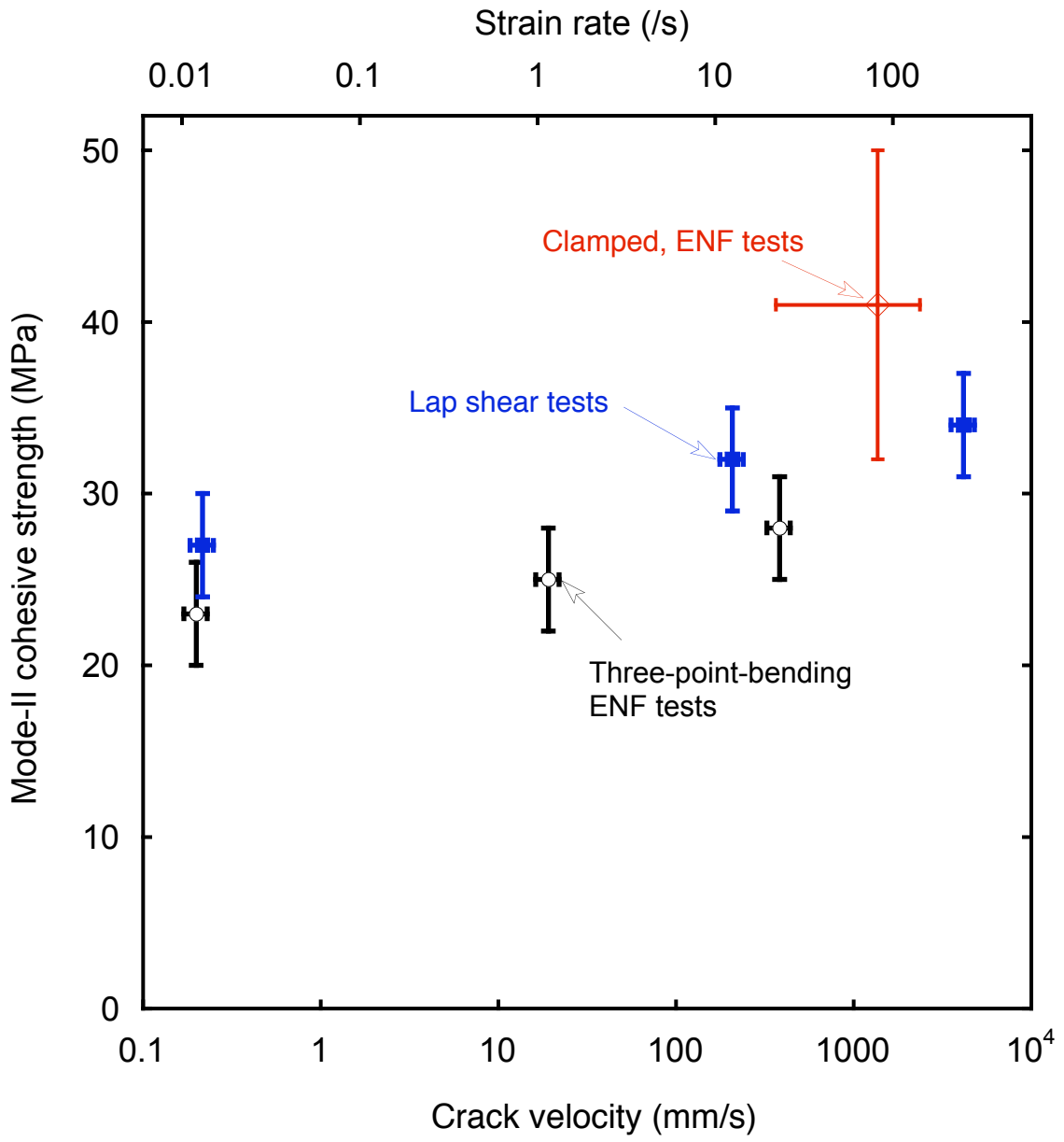

Figure 19 Mode-II cohesive strength plotted as a function of crack velocity/strain rate for the lap shear tests, three-point-bending ENF tests and the clamped ENF tests.

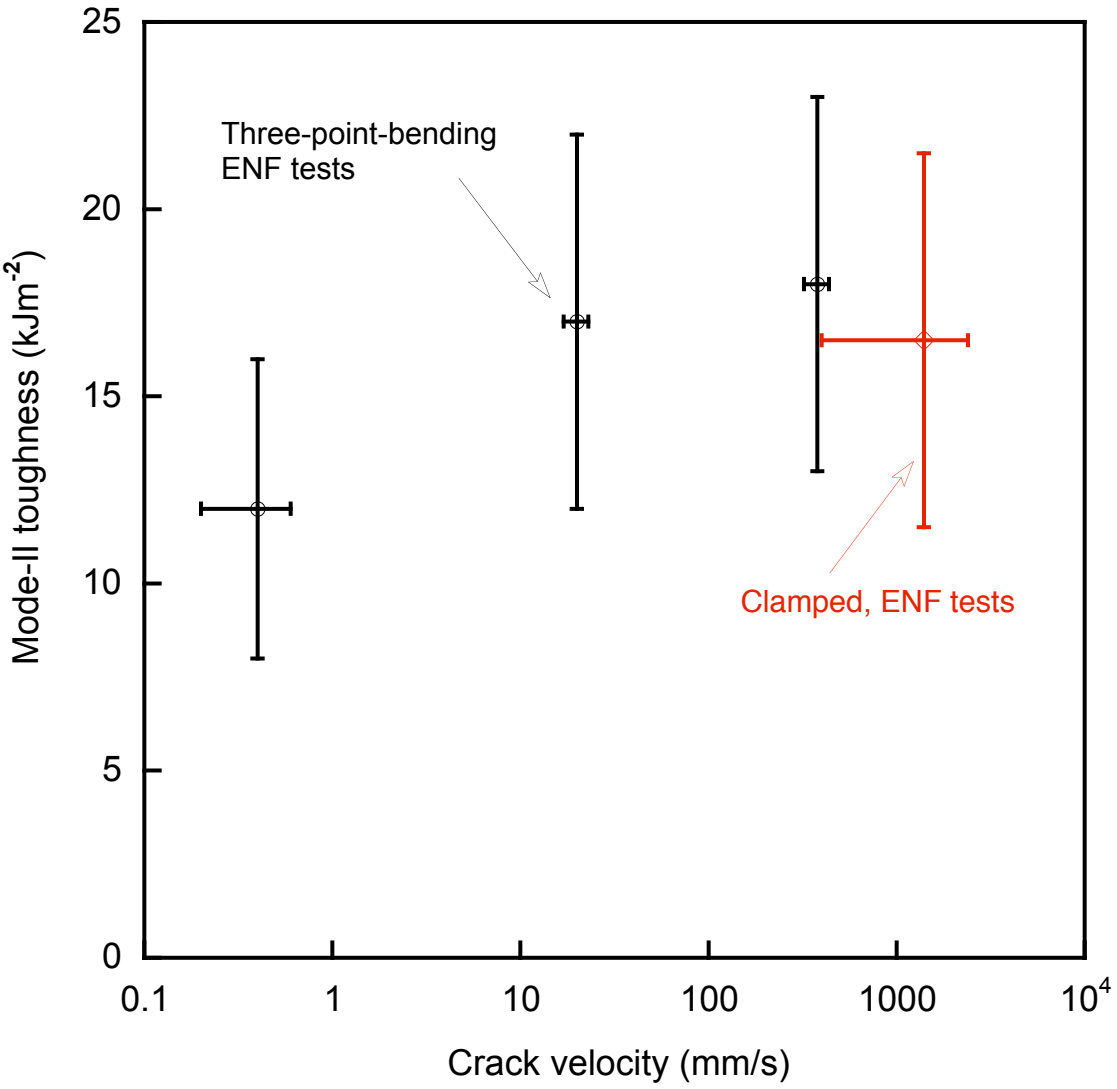

Figure 20 Mode-II toughness plotted as a function of crack velocity for both three-point-bending ENF tests and the clamped ENF tests.

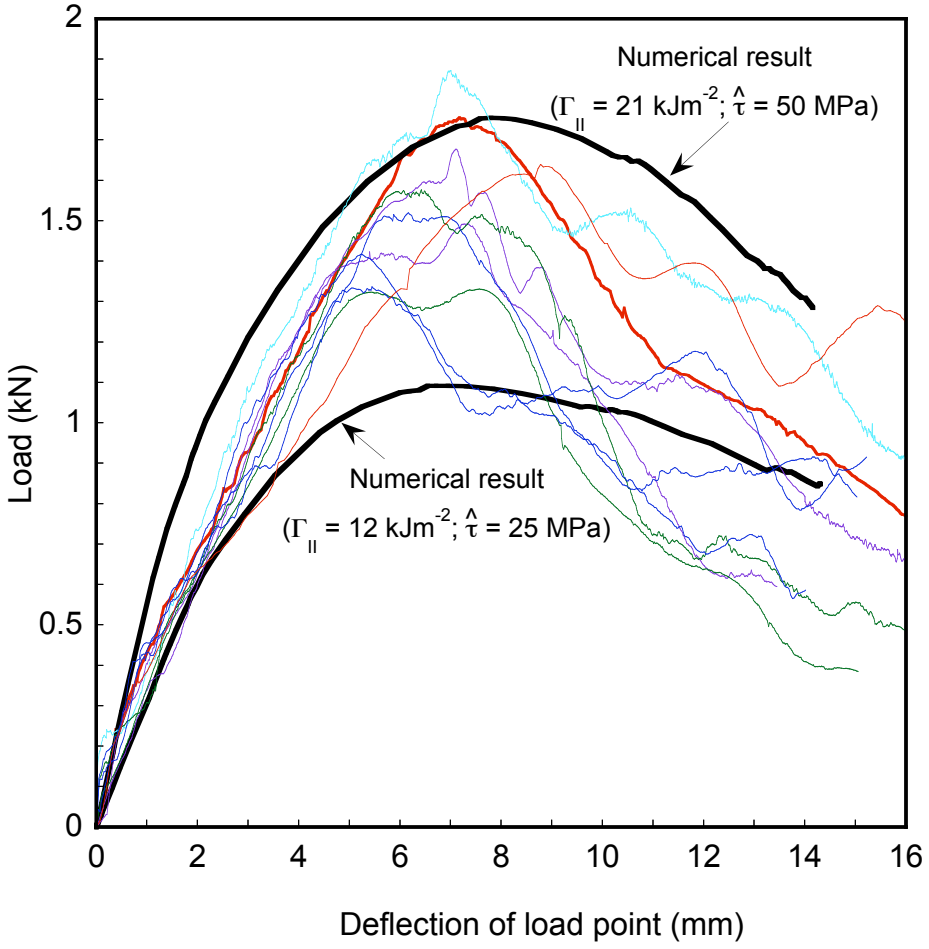

Figure 21 Comparison between experimental plots of load *versus* deflection from the clamped ENF specimens (loaded in the drop tower) and upper and lower-bound numerical predictions of the coupled-cohesive-zone model.

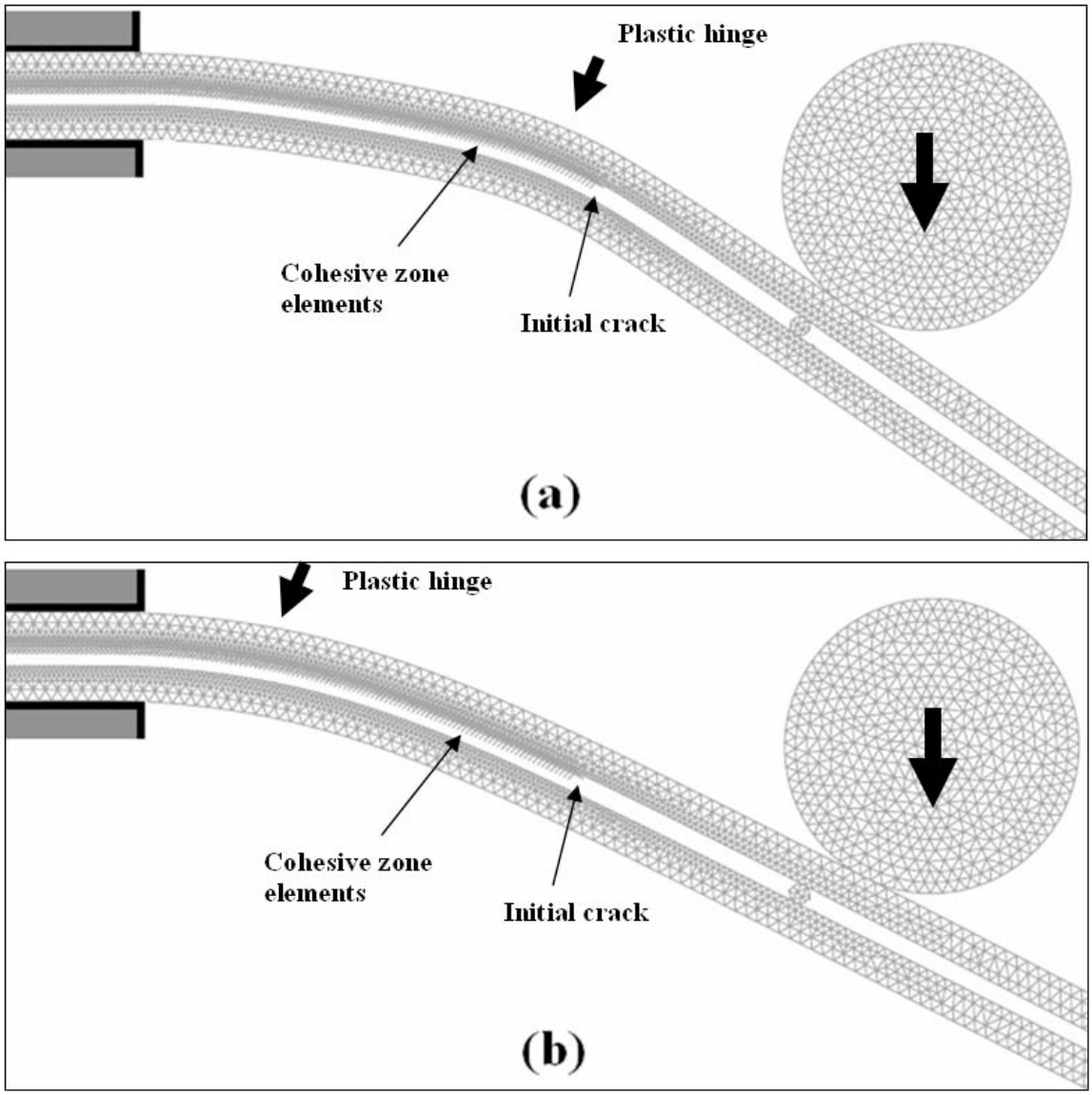

Figure 22 A comparison between the deformed shape of the clamped ENF test simulation with **(a)** upper-bound cohesive parameters ($\Gamma_{II} = 21$ kJm^{-2} and $\hat{\tau} = 45$ MPa), and **(b)** lower-bound cohesive parameters ($\Gamma_{II} = 8$ kJm^{-2} and $\hat{\tau} = 20$ MPa) with the plastic hinge formed near the clamped root of the specimen. The plastic hinge formed at the crack tip when the cohesive strength was greater than about 32 ± 3 MPa.

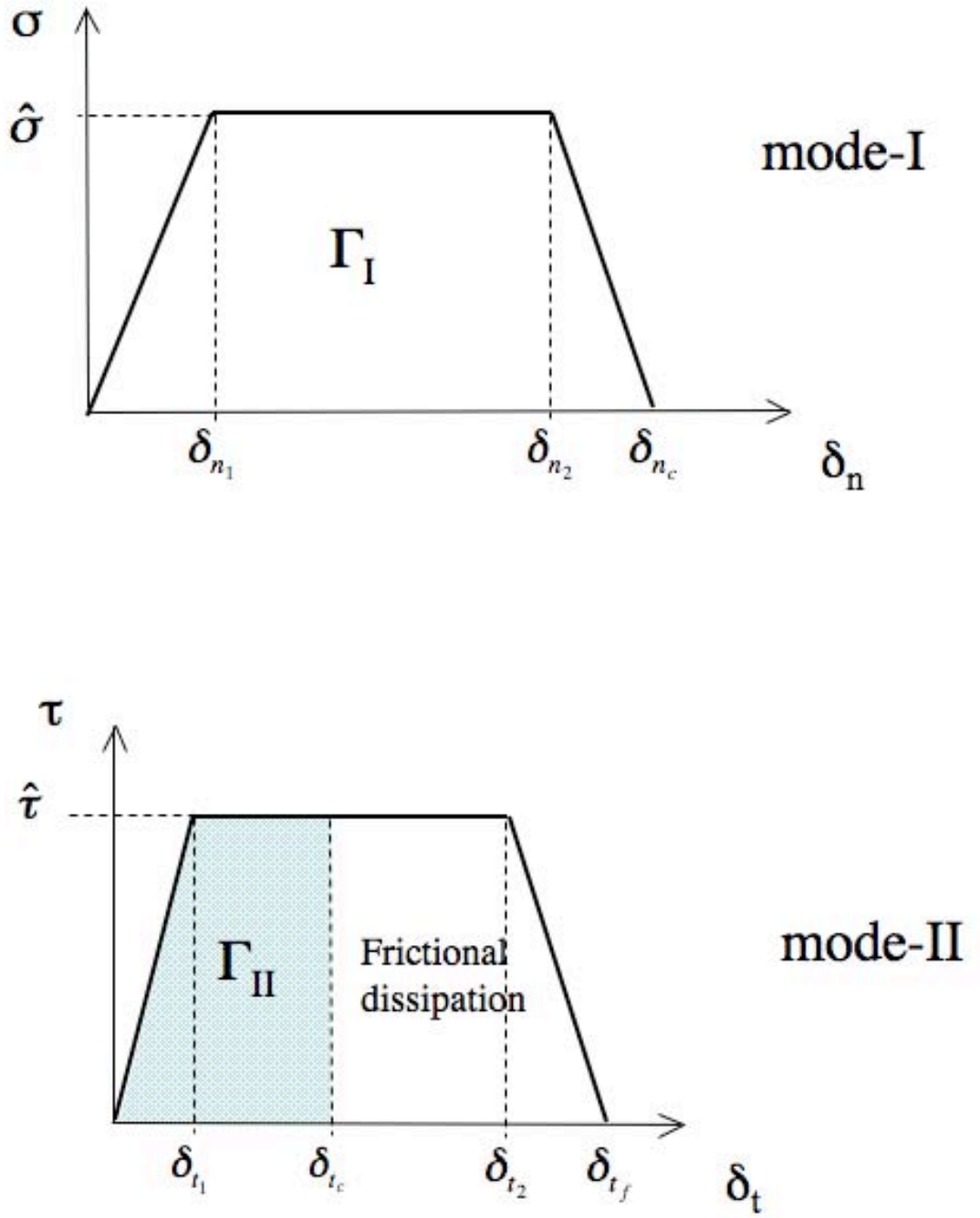

Figure A1 A trapezoidal mode-I and mode-II traction-separation law. The mode-II law illustrates the form used in this study in which there are frictional contributions to the energy dissipated at the interface.

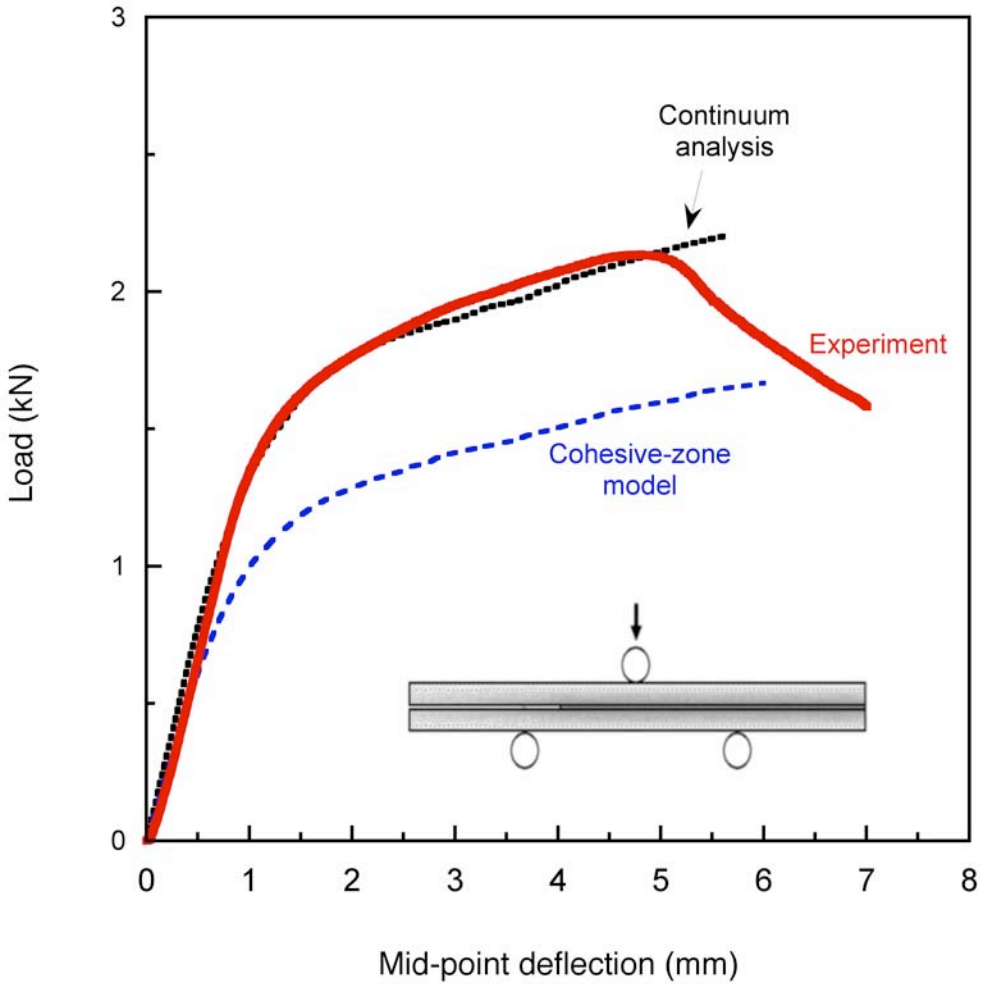

Figure A2 The numerical results from a continuum model for the load-deflection plot of the simply-supported ENF geometry of Fig. 1 agree with the experimental results of a test conducted at 0.1 mm/s up to the maximum load. However, the predictions of a cohesive-zone model, with parameters based on an approximate fit to the shear properties of the adhesive given in Fig. 16, diverge from the continuum and experimental results after a limited amount of deflection.

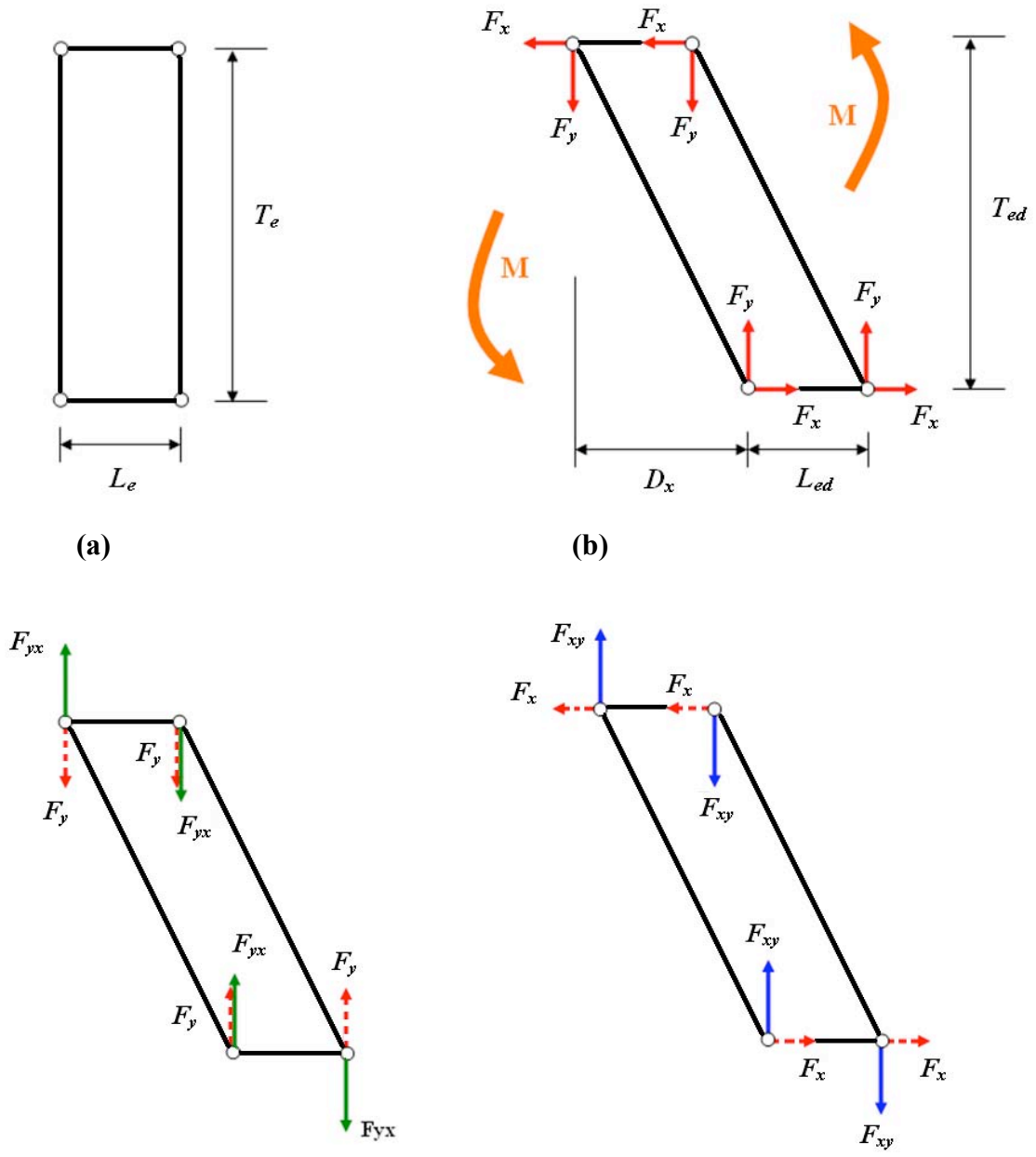

Figure A3 **(a)** An undeformed cohesive-zone element.

(b) A deformed cohesive-zone element subjected to normal and shear nodal forces, F_y and F_x respectively.

(c) Use of couple normal forces at the nodes to balancing the moment caused by the normal nodal forces.

(d) Use of couple normal forces at the nodes to balancing the moment caused by the shear nodal forces.

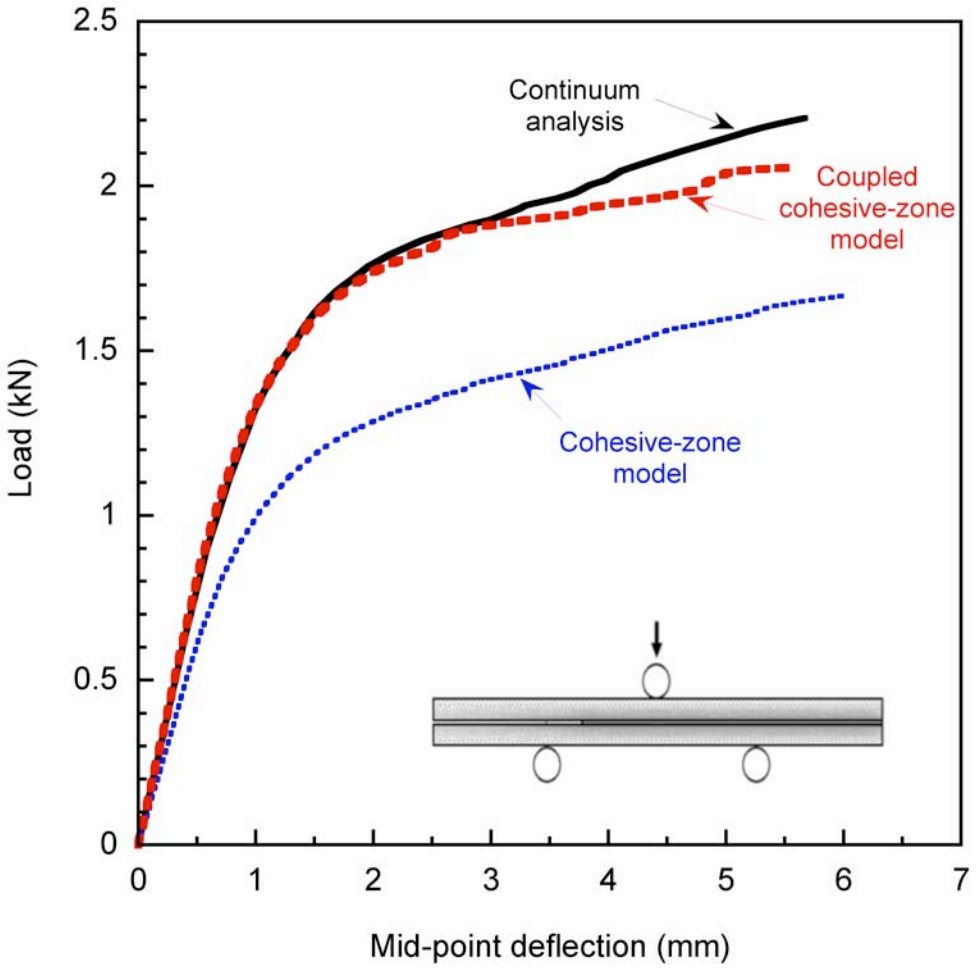

Figure A4 The coupled-cohesive-zone model provides a much better fit to the results of the continuum calculation for a simply-supported ENF specimen than does the original cohesive-zone model. The cohesive parameters for both cohesive zone models are identical in this plot.

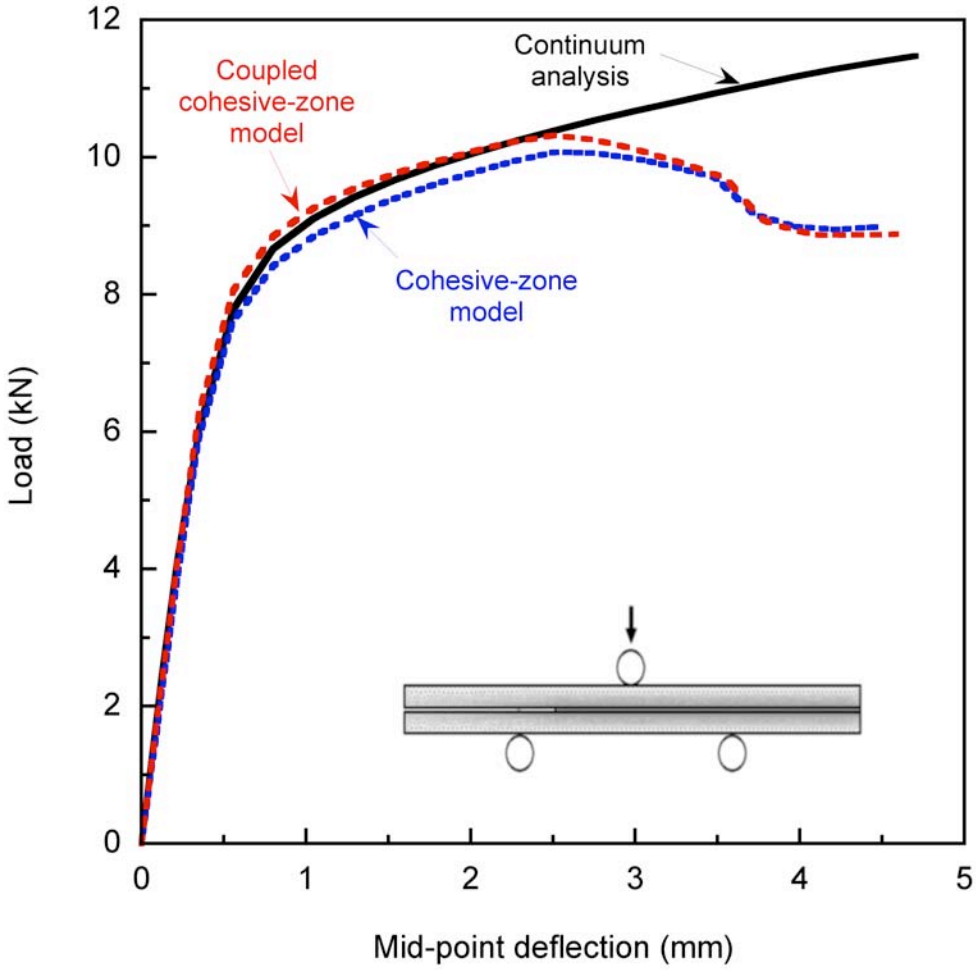

Figure A.5 Both the coupled-cohesive-zone model and the original cohesive-zone model agree with the results of the continuum calculations (while the crack does not propagate), provided the shear contributions are relatively small. The properties of the adhesive and adherend, and the cohesive parameters are identical to those used in Fig. A2, but the thickness of the adherends have been increased by a factor of three to 4.2 mm.